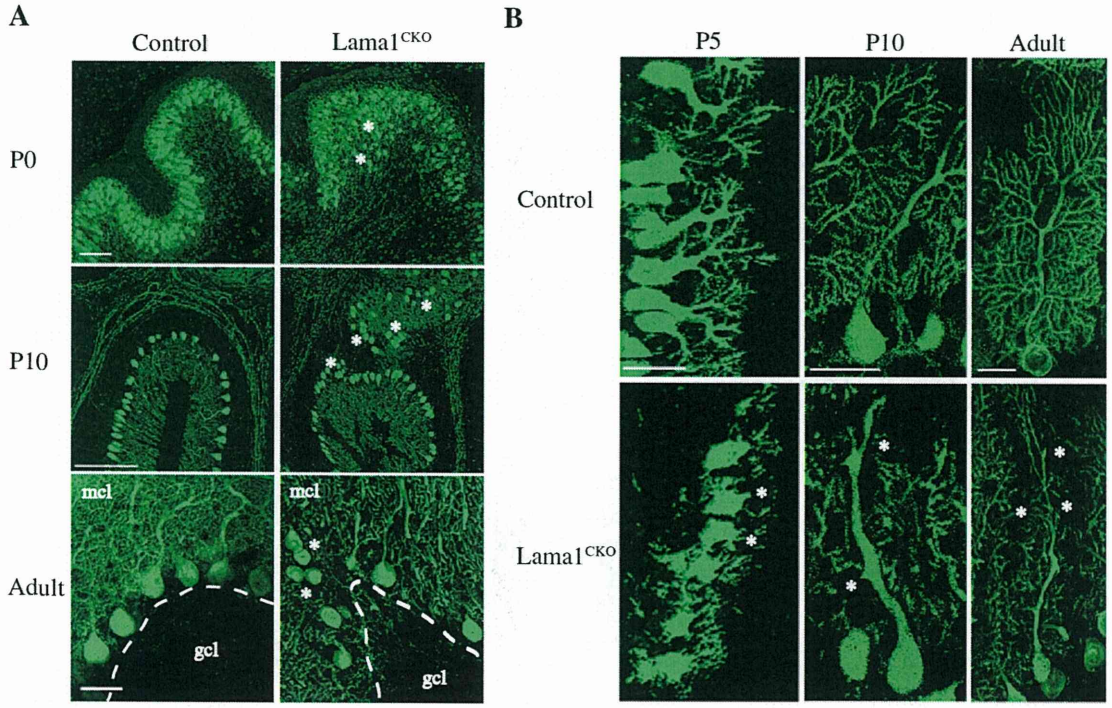

Fig. 3. Abnormal arrangement and loss of processes in Purkinje cells in Lama1^{CKO} mice. Brains from P0, P5, P10, and adult (8 weeks old) mice were cut into sections of 50 μm using a vibratome. The sections were stained with anti-calbindin D28K. Images were obtained every 2 μm at a thickness of 30 μm using a confocal laser microscope and staked using LSM510 software. (A) In the lobules of *Lama1*^{CKO} mice, the arrangement of the Purkinje cell layer between the molecular layer (mcl) and granule cell layer (gcl) was disordered at P0, P10 and adult (asterisks). Scale bars: 50 μm. (B) The branching of dendritic processes of Purkinje cells decreased remarkably in *Lama1*^{CKO} compared to control *Lama1*$^{flox/del}$ mice at P5, P10 and adult (asterisks). Scale bars: 50 μm.

that the deletion of Lama1 did not substantially affect the expression of other laminin α chains, nidogen-1, or integrin β1.

2.6. *Lama1 is critical for proliferation of granule cell precursors*

The reduced cerebellar size observed in *Lama1*^{CKO} mice might possibly result from a reduction in proliferation of granule cell precursors (GCPs) and decreased migration of proliferated GCPs. We therefore measured the number of proliferating cells in cerebellar sections from P0, P5, and P10 mice during the growth phase of the cerebellar cortex (Fig. 4A, upper panel, immunostaining of P5 cerebellum; bottom panel, quantitative data from P0, P5, and P10 cerebellums). Proliferating cells within the external granular layer (EGL) were identified by staining with phospho-histone 3 (Ser10), a marker for the M-phase of the cell cycle. We confirmed that phospho-histone 3-positive cells were GCPs by double staining with antibody to Pax6, a marker of GCPs (Fig. 4B). The number of proliferating GCPs in *Lama1*^{CKO} mice was significantly reduced during cerebellar development compared to that in control *Lama1*$^{flox/del}$ mice (Fig. 4). In addition, TUNEL assays in the cerebellum at P0, P5, P10, P21, and adulthood revealed no differences in cell death between *Lama1*^{CKO} and control mice (data not shown).

We next examined signaling molecules involved in cerebellar development. Akt is a downstream molecule of PI3-kinase and functions in both the survival and proliferation of progenitor cells in the brain (Groszer et al., 2001; Barnabe-Heider and Miller, 2003). The activation of Akt in P0 and P5 *Lama1*^{CKO} mice was significantly reduced compared to control. This reduction persisted during P0-P5, but the decrease was repaired at P10 (Fig. 5A). The expression levels of integrin β1 did not change (Fig. 5B). Integrin-linked kinase (ILK1) was increased at P0, but this increase disappeared at P5 (Fig. 5B). We also found no significant differences in the expression and phosphorylation levels of focal adhesion kinase (FAK) and Src family kinase (SFK) in the cerebellum of *Lama1*^{CKO} and control mice (Fig. 5B). These results suggest that Lama1 is essential for the proliferation of GCPs via activation of the Akt signaling pathway.

2.7. *Lama1 regulates migration of proliferating GCPs*

The abnormal cerebellar formation and granule ectopies in *Lama1*^{CKO} mice may be caused in part by defects in GCP migration. We therefore examined migration of proliferating GCPs in culture using cerebellar slices from *Lama1*^{CKO} mice, either in the absence or presence of exogenous laminin-1 (Lam-111) (Fig. 6). Sagittal slices of the cerebellum from P10 control and *Lama1*^{CKO} mice were cultured and labeled with BrdU for 30 min and stained with antibodies for Lama1 and BrdU (Fig. 6A). Lama1 was expressed in the meninges in control cerebellum slices, but was absent from *Lama1*^{CKO} cerebellum slices. The addition of exogenous laminin-1 in the culture restored Lama1 staining in the meninges of *Lama1*^{CKO} mice (Fig. 6A). BrdU-positive cells were observed in both control and *Lama1*^{CKO} mice. After three days of culture, BrdU-positive cells within the external granular layer had moved to the inner layer in control slices, whereas no cell migration was observed in *Lama1*^{CKO} slices; the BrdU-positive cells remained in the periphery (Fig. 6B). When laminin-1 was added to the culture medium of *Lama1*^{CKO} cerebellum slices, BrdU-positive cells were again able to migrate to the inner layer (Fig. 6B). Next, we used a TUNEL assay to examine whether cell death affects the migration of GCPs in a culture system. No difference was noted in the number of apoptotic cells in *Lama1*^{CKO} slices compared to control slices (Fig. 6C). We therefore concluded that the difference in the localization of BrdU-positive cells was due to defects in cell migration. These results suggest that Lama1 is essential for the migration of proliferating GCPs.

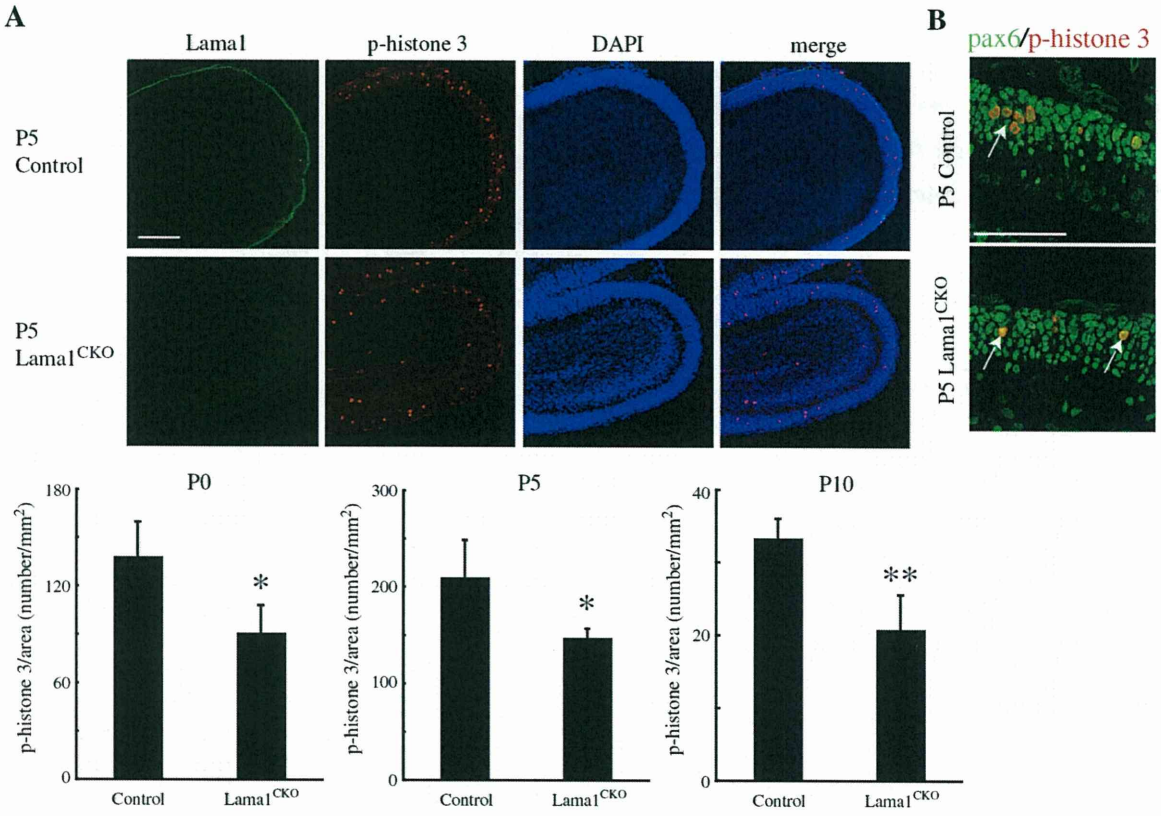

Fig. 4. Reduction in granule cell precursor (GCP) proliferation in Lama1^{CKO} mice. (A) Sagittal cerebellar sections at postnatal day 5 (P5) were analyzed by staining with phospho-histone 3 (p-H3). Proliferation of GCPs in *Lama1*^{CKO} mice was markedly decreased. Fifteen 20 μm thick sections were successively prepared from the midline of the cerebellum. The number of p-H3-positive GCPs was counted and the area of the cerebellum was measured by Image J software. The bar graph shows the mean and SD of the number of p-H3-positive cells per area (n = 5) (*, $P<0.02$, **, $P<0.005$; two-sided *t*-test). Scale bars: 100 μm. (B) Sagittal cerebellar sections at P5 were analyzed by staining with Pax6 and phospho-histone 3. Phospho-histone 3-positive cells were also positive for Pax6 (arrows). Scale bars: 50 μm.

2.8. Abnormal radial and Bergmann glial fibers in Lama1^{CKO} mice

Proliferating GCPs in the external granule layer migrate to the internal granule layer using glial guidance systems (Rakic, 1971; Edmondson and Hatten, 1987; Solecki et al., 2004). In the cerebellum, Bergmann glial cells are first seen in the cortex at the late embryonic period, and they extend their processes to the pial surface. The migration of postmitotic GCPs is guided by surface-mediated interactions with Bergmann glial fibers (Komuro and Rakic, 1998). We therefore investigated the formation of radial glial fibers at E16 and P0, and Bergmann glial fibers at P10 (this is the peak period of postmitotic GCP migration), as well as at P5 and the adult stage, by staining with antibody to radial glial cell marker-2 and glial fibrillary acidic protein (GFAP), a marker for astrocytes (Fig. 7). We found that, in *Lama1*^{CKO} mice, radial glial fibers and Bergmann glial fibers directed to the meninges were short in length and disoriented (Fig. 7A–E). Bergmann glial endfeet, which run along the meninges, were fragmented and discontinuous compared to those in control mice (Fig. 7D and E). These results suggest that distorted the layer of Purkinje cells and the reduced migration of GCPs in *Lama1*^{CKO} mice are due to impaired glial guidance and that Lama1 is required for proper glial fiber formation.

2.9. Disruption of pial basement membranes and abnormal meningeal structure

Connexin 26 (Cx26) and 43 (Cx43), gap junction family proteins, are expressed in the cerebellar arachnoid and pia of the meninges (Mercier and Hatton, 2000, 2001; Nagy et al., 2001). To delineate the role of Lama1 in the conformation of the meninges, we examined the localization of Cx26 and Cx43 by immunostaining the meninges in control and *Lama1*^{CKO} mice. We also examined the pial basement membrane by immunostaining laminin γ1 (Lamc1), which is a subunit of laminin-1 (Lama-111) and some of the other laminins, and a marker of the basement membrane. In control meninges, both Cx26 and Cx43 were expressed in the arachnoid and pia (Fig. 8Aa, b, and d). However Cx26 expression was less prominent in the arachnoid barrier (Fig. 8Ae and h, upper part) than in the arachnoid trabeculae (bottom part). Cx43 expression was nearly absent in the arachnoid of *Lama1*^{CKO} mice (Fig. 8Af and h). A thin and continuous basement layer at the bottom of the pia was stained by anti-Lamc1 antibody (arrow, Fig. 8Ac and d). The meninges of *Lama1*^{CKO} mice were thinner and the expression of both Cx26 and Cx43 was reduced (Fig. 8Ae, f, and h). The Lamc1 staining revealed that the pial basement membrane was irregular (Arrows, Fig. 8Ag and h). We also analyzed the area where granule cell ectopies were observed at the cerebellum surface, as shown in Fig. 2Ba (arrows). In the cerebellum of *Lama1*^{CKO} mice, aggregated granule cells were observed under the meninges by DAPI staining (Fig. 8Be). Some of the ectopically accumulated granule cells near the cerebellum surface were positive for Cx26 staining (Fig. 8Bd, e, and f, asterisks).

We next used electron microscopy to examine the disruption of the pial basement membrane in *Lama1*^{CKO} mice at P0 (Fig. 9A) and the adult stage (Fig. 9B). In *Lama1*^{CKO} mice, the density of glial cells was remarkably low compared with the control and no glial cells were found in the places where they were normally located in control mice (Fig. 9A, asterisk). Moreover, the pial basal lamina in *Lama1*^{CKO} was curved and discontinuous (Fig. 9A, arrows). Similar results were observed in adult mice (Fig. 9B). These results suggest that

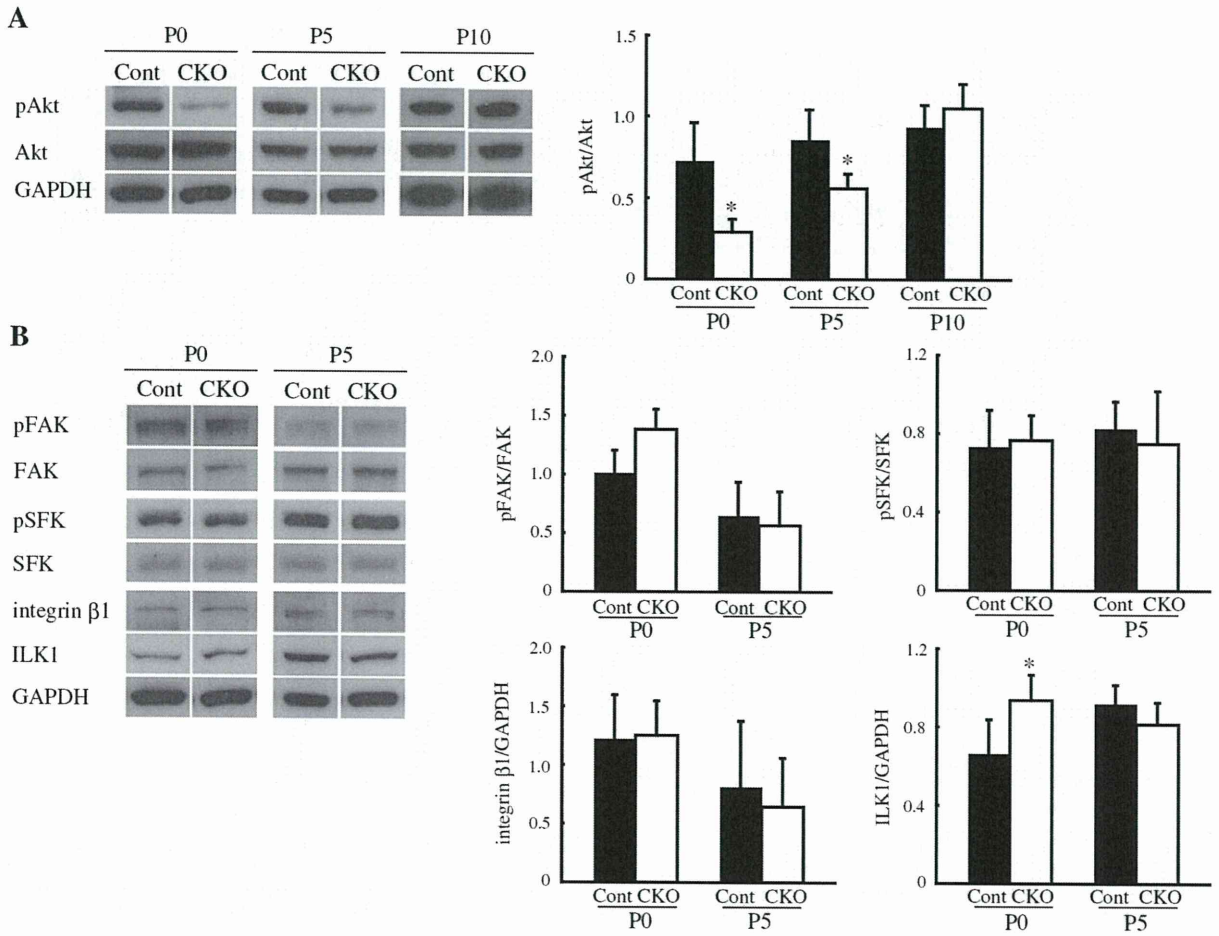

Fig. 5. Reduced proliferation signaling in Lama1^{CKO} mice. Cerebellum of control (Cont) and *Lama1*^{CKO} mice (CKO) was analyzed by immunoblotting. (A) The phosphorylated Akt level was significantly decreased at P0 and P5 in *Lama1*^{CKO} mice, compared with control mice, but this reduction was not observed at P10. (B) The expression of ILK1 was increased at P0 in *Lama1*^{CKO} mice. The activation or expression of other integrin β1-related molecules was unchanged. The bar graphs show the mean and SD, which was calculated for each signaling density (n = 5). (*, $P<0.05$; two-sided *t*-test).

Lama1 is required for the formation of the pial basement membrane and the meningeal structure.

3. Discussion

Lama1 has various biological functions, such as promotion of cell adhesion, migration, neurite outgrowth, angiogenesis, and tumor metastasis (Kleinman et al., 1990; Ekblom et al., 2003; Ichikawa et al., 2009). However, the significance of Lama1 in terms of in vivo cerebellar development and function has been difficult to elucidate because Lama1 knockout mice die in early embryonic stages (Miner et al., 2004). In this report, using conditional knockout mice for Lama1, we demonstrate that Lama1 is important for cerebellar development. Our data show that Lama1 is required for proper conformation of the meninges and for proper formation of the glial fibers.

During cerebellar development, two kinds of glial cells, radial glia and Bergmann glia, function in the migration of Purkinje cells and granule cells, which are different neuron types (Rakic, 1971; Hatten, 1999). During development, the radial glial cells disappear and are replaced by Bergmann glia until birth (Yuasa, 1996; Yuasa et al., 1996). It is conceivable that the observed defects in Bergmann glial fibers cause the aggregated granule cells under the pia and reduced GCP migration in adult *Lama1*^{CKO} mice. The interaction between GCPs and Bergmann glial fibers is necessary for GCP migration, and several adhesion molecules, such as NCAM, L1, and thrombospondin, contribute to these interactions (Chuong et al., 1987; O'Shea et al., 1990). Because laminin-1 containing Lama1 can interact with the HNK-1 carbohydrates of NCAM and L1 (Hall et al., 1997), Lama1 may be required to organize the contact between GCPs and Bergmann glia under the pia, in concert with these adhesion molecules.

Lama1 also regulates the distribution and dendritic elongation of Purkinje cells. In the mouse cerebellum, Purkinje cell precursors are generated in the primary rhombic lip between the E11 and E13 stages and these precursors migrate to the cortex along the radial glial fibers. Then, during the postnatal 3 weeks, dendrites of the Purkinje cells extend, branch, and form synapses with other neurons. Reelin, a large extracellular protein, promotes migration of Purkinje cells through radial glial guidance and lamination of Purkinje cells (Tissir and Goffinet, 2003). Since Lama1 has epidermal growth factor-like repeats similar to reelin, the abnormal lamination of Purkinje cells in *Lama1*^{CKO} mice might be due to an impaired radial glial system.

Various endogenous and microenvironmental factors, such as granule cells, growth factors, steroids, thyroid hormone, coricotroprotein-releasing factor, calcium-related molecules, PKCγ, RORα and pleiotrophin-PTPζ, are involved in dendrite formation and extension in Purkinje cells (Tanaka, 2009). Granule cells contribute to the formation of Purkinje cell dendrites via granule-Purkinje cell interactions, while electrical activity affects dendritic differentiation through calcium signaling. The

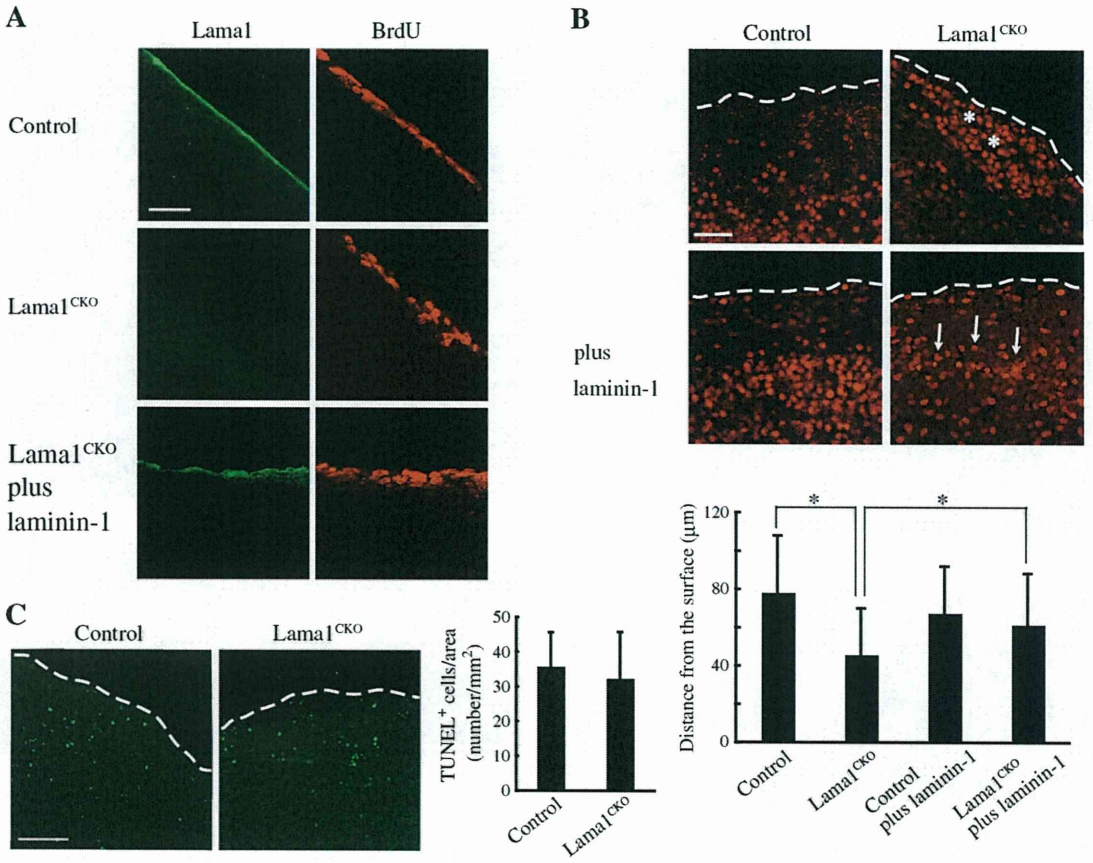

Fig. 6. Reduced migration of proliferating granule cells in Lama1^{CKO} mice. Sagittal slices of the cerebellum of P10 control and *Lama1*^{CKO} mice were labeled with bromodeoxyuridine (BrdU) and then cultured. After culture, the slices were stained with anti-BrdU antibody and anti-Lama1. (A) At 1 h after culture, lama1 was not expressed in the meninges in the slices of *Lama1*^{CKO} mice, but the expression was recovered by adding 5 μg/ml laminin-1. Scale bars: 20 μm. (B) The migration of BrdU-positive granule cells to the inner layer in *Lama1*^{CKO} mice decreased after a 72 h culture period (asterisks). However, the decrease could be rescued by adding 5 μg/ml laminin-1 (arrows). The dashed lines show the surface of the cerebellum. Scale bars: 20 μm. The bar graphs show the calculated mean and SD, (n = 500 cells). (*, $P<0.001$; two-sided *t*-test). (C) After culturing for 72 h, the slices were stained using the TUNEL method. The dashed lines show the surface of the cerebellum. No differences were observed in the number of apoptotic cells in the control or *Lama1*^{CKO} mice. The bar graphs show the calculated mean and SD. Scale bars: 100 μm.

poor dendritic formation of Purkinje cells in *Lama1*^{CKO} mice may be due to a reduction in granule cell migration and to abnormal Bergmann glial processes.

Integrin β1, α-dystroglycan, FAK, and ILK, which are receptors and signaling molecules of Lama1, are critical for the proliferation and migration of granule cells and GCPs during cerebellar development (Graus-Porta et al., 2001; Blaess et al., 2004; Mills et al., 2006; Watanabe et al., 2008). Laminin-1 is also reported to modulate sonic hedgehog (SHH) function and to increase proliferation of GCPs (Pons et al., 2001). We showed that Lama1 is essential for the proliferation and migration of GCPs. This Lama1 activity is similar to the activity of the Lama1 receptors, but the defects observed in cerebellar size and motor functions in *Lama1*^{CKO} mice were considerably more severe compared to those observed in other mutant mice. This may be because Lama1 interacts with both integrin β1 and α-dystroglycan. We found that the expression and activation of integrin β1 signaling were unchanged in *Lama1*^{CKO} mice. In contrast, the activation of Akt was transiently decreased in the *Lama1*^{CKO} cerebellum. The PI-3 kinase-Akt pathway is a signaling cascade that involves both integrin β1 and α-dystroglycan, and activation of PI-3 kinase-Akt signaling promotes neural cell proliferation and survival (Groszer et al., 2001; Barnabe-Heider and Miller, 2003). Therefore, the observed decrease in proliferation of GCPs may be due to the reduction in Akt activation at the early postnatal stages. At later stages, Akt phosphorylation levels reached normal levels, similar to those found in WT mice, probably because different external signals induced Akt activation for other cell functions, such as survival. In *Lama1*^{CKO} mice, the expression levels of Lama4 did not change, but Lama2 expression was slightly increased and Lama5 expression was reduced in the *Lama1*^{CKO} cerebellum. Double knockout mice for *Lama2* and *Lama4* showed a reduction in cortical sizes, an increase in apoptotic cells at the ventricular neuroepithelium, and detachment of radial glial cell processes in the cerebral cortex (Radakovits et al., 2009). However, these abnormalities are not observed in single gene knockouts for *Lama2* and *Lama4* (Radakovits et al., 2009). The meninges have been implicated in the regulation of radial glial survival using a slice culture that lacks the meninges (Radakovits et al., 2009) and in proper morphology of radial glia cells and migration of Cajal–Retzius cells in the cortex (Halfter et al., 2002). Lama1 deficiency resulted in discontinuous pia basement membranes (Fig. 9), although Lama2, Lama5 and nidogen were present in non-disrupted areas of the basement membrane (Supplementary material Fig. S4). These results suggest that Lama1 is required for the formation of the pial basement membrane and the meningeal structure. Thus, Lama1 may serve an important function among laminin α chains expressed in the meninges, as *Lama1*^{CKO} mice show remarkable phenotypic changes in the cerebellum following a single knockout.

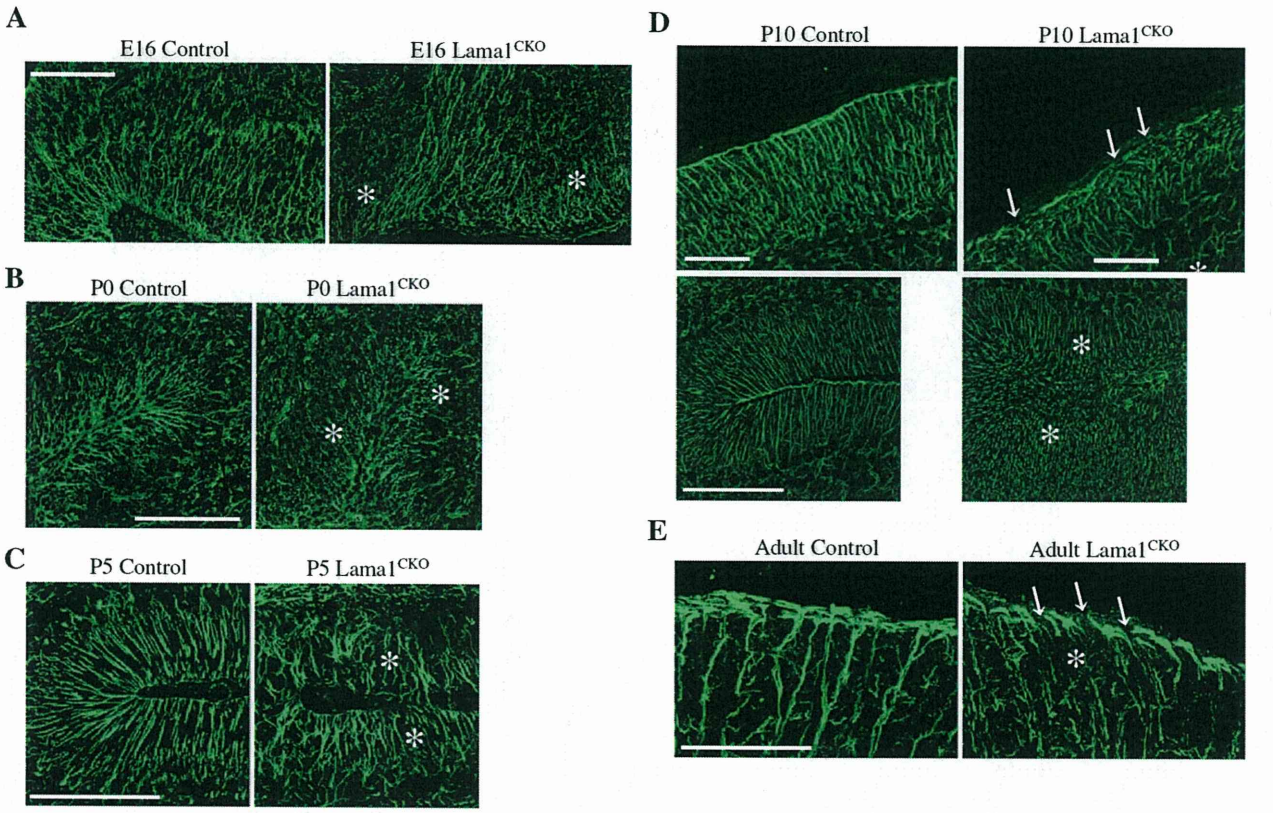

Fig. 7. Aberration of radial and Bergmann glial fibers and endfeet in Lama1^{CKO} mice. Cerebellar sections from E16 (A), P0 (B), P5 (C), P10 (D) and adult (E) mice were stained with anti-radial glial marker-2 or anti-GFAP antibody. In control mice, radial glia and Bergmann glial fibers extended to the meninges in the fissure of folia, whereas in *Lama1*^{CKO} mice, the glial fibers were discontinuous and fragmented (asterisks). (D) At the surface of the cerebellum, Bergmann glial endfeet are continuous along the meninges in control mice. Some endfeet are disrupted in *Lama1*^{CKO} mice (D and E, arrows). Scale bars: 100 μm. Scale bars: 200 μm (A and B), 50 μm (C and E), 100 μm (D).

The meninges consist of three membranous layers composed of fibroblasts, extracellular matrix, and a well-organized fluid-containing space. These membranes are the dura mater, arachnoid, and pia mater. These structures serve to protect the central nervous system and to entrap a fluid-filled space that is important for brain function and survival. In the adult brain, gap junctions are abundant in the meninges and can mediate cell–cell communication and cellular morphogenesis, proliferation, and differentiation (Nagy et al., 1997; Mercier and Hatton, 2001). Connexins (Cxs) are implicated in these biological processes through their gap junction and hemichannel activities. Cx43 is expressed in the arachnoid and pia mater of the meninges (Nagy et al., 1999). Glia-specific Cx43 knockout mice display a reduction in size of the cerebellum, granule cell ectopies, and dislamination of Purkinje cells, granule cells, and Bergmann glia (Muller et al., 1996; Clark and Barbour, 1997; Wiencken-Barger et al., 2007). Cx43 is required for cerebellum-dependent motor coordination and motor learning (Tanaka et al., 2008a, 2008b). Interestingly, these morphological defects observed in Cx43 knockout mice are similar to those seen in *Lama1*^{CKO} mice. We found that a deficiency in Lama1 results in the reduction and altered localizations of Cx43 in the cerebellum. Knockout mice for laminin 5 (Lam-332) also show altered expression and localization of Cx43 via laminin–integrin interactions in epithelial cells (Lampe et al., 1998; Isakson et al., 2006). In neuronal cells, laminin has been reported to affect the populations of postnatal neural stem and progenitor cells by altering the expression of connexins (Imbeault et al., 2009). Thus, Lama1 may be required for functional localization of connexins in the cerebellum through a similar mechanism and may have a similar function in cerebellar development.

4. Experimental procedures

4.1. Generation of conventional and conditional Lama1 knockout mice

A mouse genomic clone encoding the 5′ part of *Lama1* was isolated from a mouse 129SvJ genomic library by screening with mouse *Lama1* cDNA (Sasaki et al., 1988). A DNA fragment containing exons 14 to 18 of *Lama1* from the genomic clone was used for gene targeting. The PGKneo^{r}-PGKtk cassette from pPNT was flanked with two loxP sequences at each end and inserted into intron 15, and a third loxP sequence was cloned into intron 17 of *Lama1*. The tk-DTa cassette, which encodes the diphtheria toxin A subunit, was attached to the short arm of the targeting vector for negative selection. The *Lama1*-loxP construct (Supplementary material Fig. S1A) was linearized by *Cla*I and electroporated into R1 ES cells. The homologous recombinant cells were isolated by drug selection and transiently transfected with the CMV-cre expression plasmid (pBS185, Gibco Life Technology). Two different types of targeted ES clones were isolated, one containing the *Lama1*-deficient allele and the other containing the floxed-*Lama1* allele (Supplementary material Fig. S1A).

Two independent clones from each were injected into blastocysts to generate chimeric mice. These chimera were mated with C57BL/6 mice to generate heterozygous null (*Lama1*$^{del/+}$) or floxed-*Lama1* (*Lama1*$^{flox/+}$) mice. Genotypes of the mutant alleles were confirmed

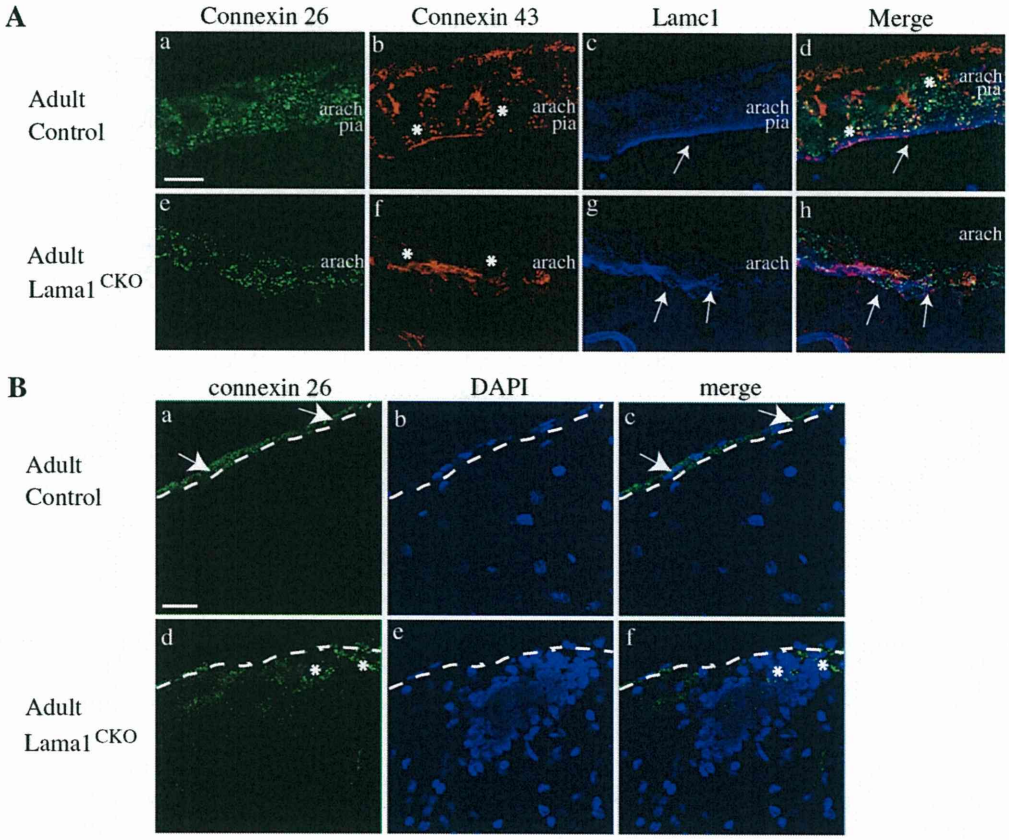

Fig. 8. Abnormal expression of connexin proteins in the meninges of *Lama1*^{CKO} mice. (A) Sagittal sections of the cerebellar surface of control (a–d) and *Lama1*^{CKO} (e–h) animals were immunostained with antibodies to connexin 26 (a and e, green), connexin 43 (b and f, red), and Lamc1 (laminin γ1, c and g, blue). Merged images in d and h. Both Cx26 and Cx43 were expressed in the arachnoid and pia of control meninges (a, b, and d). In *Lama1*^{CKO} mice, Cx26 expression was reduced in the arachnoid barrier (e and h) and Cx43 was almost entirely absent from the arachnoid (f and h, asterisks). Lamc1 was stained in a thin and continuous layer (arrows) of the pial basement membrane in control mice (c and d) but its staining was discontinuous (g and h, arrows) in *Lama1*^{CKO} mice. Scale bar: 20 μm. (B) Connexin 26 expression in granule ectopies. Sagittal sections of the cerebellar surface of control (a–c) and *Lama1*^{CKO} (d–f) mice were immunostained with antibodies to connexin 26 (green) with DAPI (blue). Cx26 puncta were present in the pial fibroblastic layer of control mice (a and c, arrows). In *Lama1*^{CKO} mice, Cx26 were stained in ectopic granule cells near the surface (d and f, asterisks). Aggregated granule cells were observed under the meninges in *Lama1*^{CKO} mice (e and f). The dashed lines show the borderline between the pial membrane and the surface of the cerebellum. Scale bar: 10 mm.

by genomic PCR and Southern blotting (Supplementary material Fig. S1B and C). These mice were further intercrossed to generate homozygous null (*Lama1*$^{del/del}$), heterozygous null/floxed (*Lama1*$^{del/flox}$), or floxed-*Lama1* (*Lama1*$^{flox/flox}$) offspring. Heterozygous *Lama1* null mice containing the *Sox2-Cre* gene (*Lama1*$^{del/+}$; *Sox2-Cre*$^{cre/+}$) were created by crossing with *Lama1*$^{del/+}$ mice with *Sox2-Cre*$^{cre/+}$ mice from The Jackson Laboratory, in which the Cre recombinase gene was inserted in the *Sox2* locus (Hayashi et al., 2002). Mice with a conditional *Lama1*-deficiency (*Lama1*^{CKO}) specifically in epiblasts were created by crossing *Lama1*$^{del/+}$ (*Sox2-Cre*$^{cre/+}$) with floxed-*Lama1* (*Lama1*$^{flox/flox}$) mice. *Lama1*$^{flox/del}$ mice developed normally and were used as controls.

Cre-mediated recombination in both null and conditional *Lama1* alleles was identified by Southern blotting and genomic PCR. DNA was prepared from mice, digested with *Xba*I, and hybridized with the probe indicated in Fig. 1A, the WT *Lama1* allele. For PCR, DNA was denatured at 95 °C for 15 min and then amplified for 30 cycles (30 s at 94 °C, 60 s at 60 °C, and 90 s at 72 °C) with ExTaq (Takara). The following primer sets were used: wild-type and floxed alleles:

E85 (5′-TACTTCAACGTGGTTAGACTTGTGCCTG-3′) and E100 (5′-ATTAGGGCTTGCTATGTCCAGAGAGACAG-3′); null allele,

E85 (5′-TACTTCAACGTGGTTAGACTTGTGCCTG-3′) and E114 (5′-TTGTGCCTTTACTAAGCCCTGCTCC-3′); cre allele, E350 (5′-AAAAT-TTGCCTGCATTACCG-3′) and E360 (5′-ATTCTCCCACCGTCAGTACG-3′). Deficiency of *Lama1* mRNA expression was confirmed by RT-PCR using E85 primer and 5′-CACACAGAGCAAATTCCATGA-3′. Both male and female mice were used for analyses.

4.2. Locomotion analyses

Mice were tested for neuropathic defects with the tail suspension test at 8–15 weeks of age. Mice were suspended for 5 min and observed. For the rotarod analysis, mice were trained for 5 min on a rod rotating at 10 rpm. This training was performed 2 times at 45-min intervals. After the training, a trial was performed on a rod that was accelerated linearly from 10 to 35 rpm over 5 min, and the time taken to fall from the rod was analyzed. The footprint analysis was modified as described previously (Karimi-Abdolrezaee et al., 2006). The mice were trained to walk on a narrow paper-covered runway (50 cm long and 5.5 cm wide). Their forelimbs and hindlimbs were dipped in black and red ink, respectively, and the mice walked on the paper 3 times. For the measurements, the first and last 10 cm of

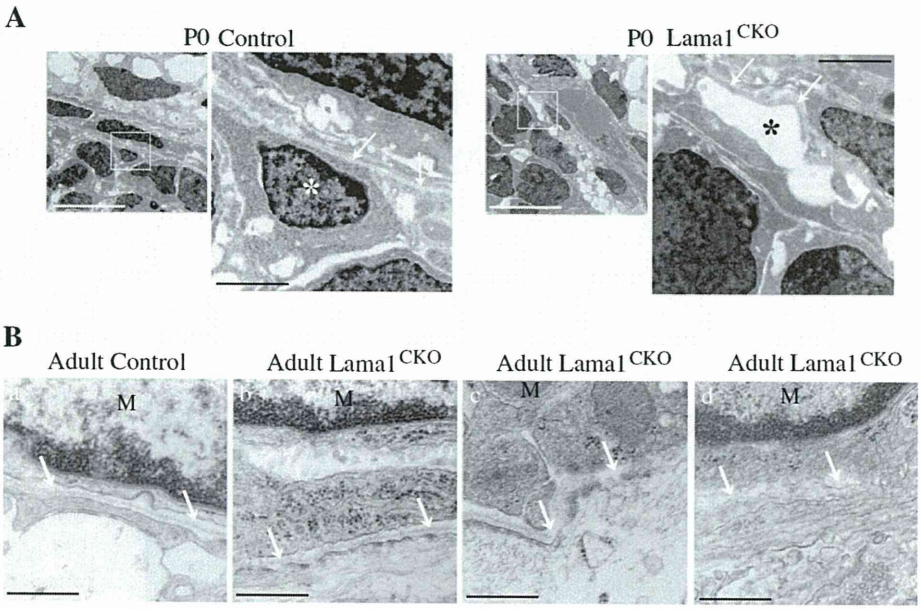

Fig. 9. Disruption of the pial basement membranes in Lama1^{CKO} mice. (A) Electron micrographs of the cerebellar surface of mice at P0. White boxed areas are enlarged in the right panels. In *Lama1*^{CKO} mice, the density of glial cells was remarkably low compared with that of the control mice (white and black asterisk). The pial basal lamina of *Lama1*^{CKO} mice was distorted, curved and discontinuous (arrows). White scale bar: 10 μm, Black scale bar: 2 μm. (B) Electron micrograph of the cerebellar surface of adult mice. Control (a) and *Lama1*^{CKO} mice (b–d). The pial basal lamina in *Lama1*^{CKO} mice was often irregular (b, arrows), disorganized (c, arrows) and discontinuous (d, arrows). M: Meningeal cells. Scale bar: 500 nm.

the prints were excluded. If the mouse stopped in the middle of the track, the trial was repeated. The data were analyzed by calculating the average of all steps per print in all trials.

4.3. Histological analysis

Mice at 8 weeks age were fixed by perfusion with 4% paraformaldehyde (PFA) under anesthesia. Samples of brain tissue were fixed in 4% PFA and embedded in paraffin. Sections (4 μm thick) were deparaffinized with xylene, hydrated in a graded series of ethanol, and washed with PBS. Tissue sections were stained with Luxol Fast Blue.

4.4. Immunohistochemistry

The brains were fixed with 4% PFA in 0.1 M PBS, pH 7.4 overnight at 4 °C and then cryoprotected in 30% sucrose in PBS for 72 h at 4 °C. Sections (20 μm) were cut with a cryostat and mounted onto glass slides. For calbindin staining, the brain was again fixed by perfusion with 4% PFA in 0.1 M PBS, pH 7.4 but sections (50 μm) were prepared using a vibratome. For immunostaining, the frozen sections were air-dried and washed with PBS. The paraffin-embedded sections were deparaffinized and incubated with either proteinase K (DAKO) for GFAP or 10 mM citrate buffer, pH 6.0 under microwave irradiation. The sections were incubated with 0.1% Triton X-100 in PBS for 15 min. After washing, the sections were blocked with blocking buffer (5% normal donkey serum and 2% BSA in PBS) for 30 min, and incubated with dilutions of the primary antibody in the blocking buffer overnight at 4 °C. The following primary antibodies were used: rabbit anti-laminin α1 (Lama1) (Sasaki et al., 2002); rabbit anti-laminin α2 (Lama2), rabbit anti-laminin α3 (Lama3), rabbit anti-laminin α4 (Lama4), rabbit anti-laminin α5 (Lama5) (a gift from Dr. Sasaki); rat anti-nidogen-1 (Millipore); mouse anti-phospho-histone 3 (Ser10)(Cell Signaling); rat anti-BrdU (Serotec); rabbit anti-GFAP (DAKO); rabbit anti-Pax6 (Covance); mouse anti-radial glial cell marker-2 (Millipore) and anti-calbindin D28K (Millipore). The slides were washed with PBS and incubated with the secondary antibodies, Alexa 488 donkey anti-rabbit (Molecular Probes), Cy3 donkey anti-mouse, and Cy3 donkey anti-rat (Jackson Immuno) for 1 h. The slides were washed with PBS, coverslipped with mounting medium containing DAPI, and observed using a Zeiss 510 confocal laser microscope. For connexin staining, the frozen sections were fixed in acetone and incubated with primary antibodies in 0.2% gelatin PBS for 3 h. The primary antibodies included rabbit anti-connexin 26 (Invitrogen), monoclonal mouse anti-connexin 43 (Invitrogen), and rat monoclonal anti-laminin γ1 (Lamc1) chain (Millipore). The secondary antibodies were AlexaFluor 488 goat anti-rabbit, AlexaFluor 488 and 546 goat anti-mouse (Invitrogen), and Cy™5-conjugated donkey anti-rat (Jackson ImmunoResearch Laboratories) and were incubated for 1 h. In each experiment, several sections were incubated without the primary antibody to serve as controls. When the primary antibody was omitted from the staining, no immunoreactivity was observed.

4.5. Slice culture

Slice culture of cerebellum tissue was established as described previously (Streit et al., 1993). Cerebella from postnatal day 10 (P10) mice were sliced into 300 μm thick pieces using a tissue chopper (Muromachi Kikai Co., Ltd). The slices were put onto Millicell tissue culture inserts (Millipore) and incubated with 5 mM bromodeoxyuridine (BrdU) in culture medium comprising 50% Minimum essential medium, 25% Hanks' balanced salt solution, and 25% horse serum (Invitrogen) for 30 min at 37 °C in 5% CO_2. The slices were washed with the culture medium and cultured with or without 5 μg/ml laminin-1 (Sigma). After incubation, the slices were frozen and cut in a sagittal orientation. The sections were fixed with 4% PFA in 0.1 M PBS, pH 7.4, and incubated with 0.5% Triton X-100 in PBS for 15 min. The sections were subsequently incubated with 2 N HCl for 30 min at 37 °C, neutralized with 0.1 M borate buffer for 10 min and then stained as described above.

4.6. Western blotting

Lysate from the cerebellum was prepared in 50 mM Tris–HCl, 150 mM NaCl, 1 mM EDTA, 1 mM EGTA, 1% Triton X-100, 1.5 mM $MgCl_2$, 10% glycerol, complete mini protease inhibitor mixture (Roche), 1 mM PMSF, 1 mM Na_3VO_4, and 10 mM NaF, pH 7.4. The lysate was subjected to SDS-PAGE using 4–12% gradient gels (Invitrogen). For immunoblotting, the gels were transferred onto PVDF membranes, blocked with 5% non-fat milk (Cell Signaling), and incubated with primary antibodies in 5% BSA overnight at 4 °C. The primary antibodies used were mouse anti-phospho Akt (Ser473), rabbit anti-Akt, phospho-Src family kinase (Tyr416), rabbit anti-ILK1 (Cell Signaling), rabbit anti-FAK (Tyr397), mouse anti-FAK, mouse anti-GAPDH, mouse anti-Src family kinase (Millipore), and rabbit anti-integrin β1 (Santa Cruz).

4.7. Electron microscopy

The cerebellum of P0 mice was dissected and fixed with 2.5% glutaraldehyde in phosphate buffer (pH 7.4). The cerebellum of adult mice was dissected and perfusion-fixed with 2% PFA/2% glutaraldehyde in phosphate buffer (pH 7.4). The cerebellum was postfixed with 1% OsO_4 in PBS for 1 h at 4 °C, dehydrated through a graded series of ethanol, and embedded in epoxy resin. Ultrathin sections were stained with 4% uranyl acetate and lead citrate and then examined with a JEM1230 (JOEL) electron microscope.

4.8. Statistical analyses

Data are presented as the mean and SD. The minimum level of statistical significance was set at $P=0.05$. Differences were analyzed using the two-sided Student's t test with unequal variance.

Supplementary materials related to this article can be found online at doi:10.1016/j.matbio.2011.09.002.

Acknowledgments

We thank Glenn Longenecker and Ashok B. Kulkarni for their help in creating the mutant mice, Takako Sasaki for the laminin α1 antibody, and Hynda K. Kleinman for critical reading. This work was supported by the Intramural Program of the NIDCR, National Institutes of Health (Y.Y.) and grants from the Ministry of Education, Culture, Sports Science and Technology of Japan (17082008 and 2230023 to E. A-H.).

References

Alpy, F., Jivkov, I., Sorokin, L., Klein, A., Arnold, C., Huss, Y., Kedinger, M., Simon-Assmann, P., Lefebvre, O., 2005. Generation of a conditionally null allele of the laminin alpha1 gene. Genesis 43, 59–70.

Andrae, J., Afink, G., Zhang, X.Q., Wurst, W., Nister, M., 2004. Forced expression of platelet-derived growth factor B in the mouse cerebellar primordium changes cell migration during midline fusion and causes cerebellar ectopia. Mol. Cell. Neurosci. 26, 308–321.

Aumailley, M., Bruckner-Tuderman, L., Carter, W.G., Deutzmann, R., Edgar, D., Ekblom, P., Engel, J., Engvall, E., Hohenester, E., Jones, J.C., Kleinman, H.K., Marinkovich, M.P., Martin, G.R., Mayer, U., Meneguzzi, G., Miner, J.H., Miyazaki, K., Patarroyo, M., Paulsson, M., Quaranta, V., Sanes, J.R., Sasaki, T., Sekiguchi, K., Sorokin, L.M., Talts, J.F., Tryggvason, K., Uitto, J., Virtanen, I., von der Mark, K., Wewer, U.M., Yamada, Y., Yurchenco, P.D., 2005. A simplified laminin nomenclature. Matrix Biol. 24, 326–332.

Barnabe-Heider, F., Miller, F.D., 2003. Endogenously produced neurotrophins regulate survival and differentiation of cortical progenitors via distinct signaling pathways. J. Neurosci. 23, 5149–5160.

Blaess, S., Graus-Porta, D., Belvindrah, R., Radakovits, R., Pons, S., Littlewood-Evans, A., Senften, M., Guo, H., Li, Y., Miner, J.H., Reichardt, L.F., Muller, U., 2004. Beta1-integrins are critical for cerebellar granule cell precursor proliferation. J. Neurosci. 24, 3402–3412.

Chuong, C.M., Crossin, K.L., Edelman, G.M., 1987. Sequential expression and differential function of multiple adhesion molecules during the formation of cerebellar cortical layers. J. Cell Biol. 104, 331–342.

Clark, B.A., Barbour, B., 1997. Currents evoked in Bergmann glial cells by parallel fibre stimulation in rat cerebellar slices. J. Physiol. 502 (Pt 2), 335–350.

Edmondson, J.C., Hatten, M.E., 1987. Glial-guided granule neuron migration in vitro: a high-resolution time-lapse video microscopic study. J. Neurosci. 7, 1928–1934.

Edwards, M.M., Mammadova-Bach, E., Alpy, F., Klein, A., Hicks, W.L., Roux, M., Simon-Assmann, P., Smith, R.S., Orend, G., Wu, J., Peachey, N.S., Naggert, J.K., Lefebvre, O., Nishina, P.M., 2010. Mutations in Lama1 disrupt retinal vascular development and inner limiting membrane formation. J. Biol. Chem. 285, 7697–7711.

Ekblom, P., Lonai, P., Talts, J.F., 2003. Expression and biological role of laminin-1. Matrix Biol. 22, 35–47.

Goldowitz, D., Hamre, K., 1998. The cells and molecules that make a cerebellum. Trends Neurosci. 21, 375–382.

Graus-Porta, D., Blaess, S., Senften, M., Littlewood-Evans, A., Damsky, C., Huang, Z., Orban, P., Klein, R., Schittny, J.C., Muller, U., 2001. Beta1-class integrins regulate the development of laminae and folia in the cerebral and cerebellar cortex. Neuron 31, 367–379.

Groszer, M., Erickson, R., Scripture-Adams, D.D., Lesche, R., Trumpp, A., Zack, J.A., Kornblum, H.I., Liu, X., Wu, H., 2001. Negative regulation of neural stem/progenitor cell proliferation by the Pten tumor suppressor gene in vivo. Science 294, 2186–2189.

Gullberg, D., Ekblom, P., 1995. Extracellular matrix and its receptors during development. Int. J. Dev. Biol. 39, 845–854.

Halfter, W., Dong, S., Yip, Y.P., Willem, M., Mayer, U., 2002. A critical function of the pial basement membrane in cortical histogenesis. J. Neurosci. 22, 6029–6040.

Hall, H., Carbonetto, S., Schachner, M., 1997. L1/HNK-1 carbohydrate- and beta 1 integrin-dependent neural cell adhesion to laminin-1. J. Neurochem. 68, 544–553.

Hatten, M.E., 1999. Central nervous system neuronal migration. Annu. Rev. Neurosci. 22, 511–539.

Hayashi, S., Lewis, P., Pevny, L., McMahon, A.P., 2002. Efficient gene modulation in mouse epiblast using a Sox2Cre transgenic mouse strain. Mech. Dev. 119 (Suppl. 1), S97–S101.

Herrup, K., Kuemerle, B., 1997. The compartmentalization of the cerebellum. Annu. Rev. Neurosci. 20, 61–90.

Ichikawa, N., Iwabuchi, K., Kurihara, H., Ishii, K., Kobayashi, T., Sasaki, T., Hattori, N., Mizuno, Y., Hozumi, K., Yamada, Y., Arikawa-Hirasawa, E., 2009. Binding of laminin-1 to monosialoganglioside GM1 in lipid rafts is crucial for neurite outgrowth. J. Cell Sci. 122, 289–299.

Imbeault, S., Gauvin, L.G., Toeg, H.D., Pettit, A., Sorbara, C.D., Migahed, L., DesRoches, R., Menzies, A.S., Nishii, K., Paul, D.L., Simon, A.M., Bennett, S.A., 2009. The extracellular matrix controls gap junction protein expression and function in postnatal hippocampal neural progenitor cells. BMC Neurosci. 10, 13.

Isakson, B.E., Olsen, C.E., Boitano, S., 2006. Laminin-332 alters connexin profile, dye coupling and intercellular Ca2+ waves in ciliated tracheal epithelial cells. Respir. Res. 7, 105.

Karimi-Abdolrezaee, S., Eftekharpour, E., Wang, J., Morshead, C.M., Fehlings, M.G., 2006. Delayed transplantation of adult neural precursor cells promotes remyelination and functional neurological recovery after spinal cord injury. J. Neurosci. 26, 3377–3389.

Kleinman, H.K., Sephel, G.C., Tashiro, K., Weeks, B.S., Burrous, B.A., Adler, S.H., Yamada, Y., Martin, G.R., 1990. Laminin in neuronal development. Ann. N. Y. Acad. Sci. 580, 302–310.

Komuro, H., Rakic, P., 1998. Distinct modes of neuronal migration in different domains of developing cerebellar cortex. J. Neurosci. 18, 1478–1490.

Lampe, P.D., Nguyen, B.P., Gil, S., Usui, M., Olerud, J., Takada, Y., Carter, W.G., 1998. Cellular interaction of integrin alpha3beta1 with laminin 5 promotes gap junctional communication. J. Cell Biol. 143, 1735–1747.

Li, S., Edgar, D., Fassler, R., Wadsworth, W., Yurchenco, P.D., 2003. The role of laminin in embryonic cell polarization and tissue organization. Dev. Cell 4, 613–624.

Li, S., Liquari, P., McKee, K.K., Harrison, D., Patel, R., Lee, S., Yurchenco, P.D., 2005. Laminin-sulfatide binding initiates basement membrane assembly and enables receptor signaling in Schwann cells and fibroblasts. J. Cell Biol. 169, 179–189.

Mercier, F., Hatton, G.I., 2000. Immunocytochemical basis for a meningeo-glial network. J. Comp. Neurol. 420, 445–465.

Mercier, F., Hatton, G.I., 2001. Connexin 26 and basic fibroblast growth factor are expressed primarily in the subpial and subependymal layers in adult brain parenchyma: roles in stem cell proliferation and morphological plasticity? J. Comp. Neurol. 431, 88–104.

Mills, J., Niewmierzycka, A., Oloumi, A., Rico, B., St-Arnaud, R., Mackenzie, I.R., Mawji, N.M., Wilson, J., Reichardt, L.F., Dedhar, S., 2006. Critical role of integrin-linked kinase in granule cell precursor proliferation and cerebellar development. J. Neurosci. 26, 830–840.

Miner, J.H., Yurchenco, P.D., 2004. Laminin functions in tissue morphogenesis. Annu. Rev. Cell Dev. Biol. 20, 255–284.

Miner, J.H., Li, C., Mudd, J.L., Go, G., Sutherland, A.E., 2004. Compositional and structural requirements for laminin and basement membranes during mouse embryo implantation and gastrulation. Development 131, 2247–2256.

Muller, T., Moller, T., Neuhaus, J., Kettenmann, H., 1996. Electrical coupling among Bergmann glial cells and its modulation by glutamate receptor activation. Glia 17, 274–284.

Nagy, J.I., Ochalski, P.A., Li, J., Hertzberg, E.L., 1997. Evidence for the co-localization of another connexin with connexin-43 at astrocytic gap junctions in rat brain. Neuroscience 78, 533–548.

Nagy, J.I., Patel, D., Ochalski, P.A., Stelmack, G.L., 1999. Connexin30 in rodent, cat and human brain: selective expression in gray matter astrocytes, co-localization with connexin43 at gap junctions and late developmental appearance. Neuroscience 88, 447–468.

Nagy, J.I., Li, X., Rempel, J., Stelmack, G., Patel, D., Staines, W.A., Yasumura, T., Rash, J.E., 2001. Connexin26 in adult rodent central nervous system: demonstration at

astrocytic gap junctions and colocalization with connexin30 and connexin43. J. Comp. Neurol. 441, 302–323.
O'Shea, K.S., Rheinheimer, J.S., Dixit, V.M., 1990. Deposition and role of thrombospondin in the histogenesis of the cerebellar cortex. J. Cell Biol. 110, 1275–1283.
Pons, S., Trejo, J.L., Martinez-Morales, J.R., Marti, E., 2001. Vitronectin regulates Sonic hedgehog activity during cerebellum development through CREB phosphorylation. Development 128, 1481–1492.
Qu, Q., Smith, F.I., 2004. Alpha-dystroglycan interactions affect cerebellar granule neuron migration. J. Neurosci. Res. 76, 771–782.
Radakovits, R., Barros, C.S., Belvindrah, R., Patton, B., Muller, U., 2009. Regulation of radial glial survival by signals from the meninges. J. Neurosci. 29, 7694–7705.
Rakic, P., 1971. Neuron–glia relationship during granule cell migration in developing cerebellar cortex. A Golgi and electronmicroscopic study in *Macacus rhesus*. J. Comp. Neurol. 141, 283–312.
Rakic, P., Sidman, R.L., 1973. Weaver mutant mouse cerebellum: defective neuronal migration secondary to abnormality of Bergmann glia. Proc. Natl. Acad. Sci. U.S.A. 70, 240–244.
Sasaki, M., Kleinman, H.K., Huber, H., Deutzmann, R., Yamada, Y., 1988. Laminin, a multidomain protein. The A chain has a unique globular domain and homology with the basement membrane proteoglycan and the laminin B chains. J. Biol. Chem. 263, 16536–16544.
Sasaki, T., Giltay, R., Talts, U., Timpl, R., Talts, J.F., 2002. Expression and distribution of laminin alpha1 and alpha2 chains in embryonic and adult mouse tissues: an immunochemical approach. Exp. Cell Res. 275, 185–199.
Satz, J.S., Ostendorf, A.P., Hou, S., Turner, A., Kusano, H., Lee, J.C., Turk, R., Nguyen, H., Ross-Barta, S.E., Westra, S., Hoshi, T., Moore, S.A., Campbell, K.P., 2010. Distinct functions of glial and neuronal dystroglycan in the developing and adult mouse brain. J. Neurosci. 30, 14560–14572.
Scheele, S., Falk, M., Franzen, A., Ellin, F., Ferletta, M., Lonai, P., Andersson, B., Timpl, R., Forsberg, E., Ekblom, P., 2005. Laminin alpha1 globular domains 4–5 induce fetal development but are not vital for embryonic basement membrane assembly. Proc. Natl. Acad. Sci. U.S.A. 102, 1502–1506.
Smyth, N., Vatansever, H.S., Murray, P., Meyer, M., Frie, C., Paulsson, M., Edgar, D., 1999. Absence of basement membranes after targeting the LAMC1 gene results in embryonic lethality due to failure of endoderm differentiation. J. Cell Biol. 144, 151–160.
Solecki, D.J., Model, L., Gaetz, J., Kapoor, T.M., Hatten, M.E., 2004. Par6alpha signaling controls glial-guided neuronal migration. Nat. Neurosci. 7, 1195–1203.
Sotelo, C., 2004. Cellular and genetic regulation of the development of the cerebellar system. Prog. Neurobiol. 72, 295–339.
Streit, A., Nolte, C., Rasony, T., Schachner, M., 1993. Interaction of astrochondrin with extracellular matrix components and its involvement in astrocyte process formation and cerebellar granule cell migration. J. Cell Biol. 120, 799–814.
Tanaka, M., 2009. Dendrite formation of cerebellar purkinje cells. Neurochem. Res. 34, 2078–2088.
Tanaka, M., Yamaguchi, K., Tatsukawa, T., Nishioka, C., Nishiyama, H., Theis, M., Willecke, K., Itohara, S., 2008a. Lack of Connexin43-mediated bergmann glial gap junctional coupling does not affect cerebellar long-term depression, motor coordination, or eyeblink conditioning. Front. Behav. Neurosci. 2, 1.
Tanaka, M., Yamaguchi, K., Tatsukawa, T., Theis, M., Willecke, K., Itohara, S., 2008b. Connexin43 and bergmann glial gap junctions in cerebellar function. Front. Neurosci. 2, 225–233.
Tissir, F., Goffinet, A.M., 2003. Reelin and brain development. Nat. Rev. Neurosci. 4, 496–505.
Watanabe, F., Miyazaki, T., Takeuchi, T., Fukaya, M., Nomura, T., Noguchi, S., Mori, H., Sakimura, K., Watanabe, M., Mishina, M., 2008. Effects of FAK ablation on cerebellar foliation, Bergmann glia positioning and climbing fiber territory on Purkinje cells. Eur. J. Neurosci. 27, 836–854.
Wiencken-Barger, A.E., Djukic, B., Casper, K.B., McCarthy, K.D., 2007. A role for Connexin43 during neurodevelopment. Glia 55, 675–686.
Yuasa, S., 1996. Bergmann glial development in the mouse cerebellum as revealed by tenascin expression. Anat. Embryol. (Berl) 194, 223–234.
Yuasa, S., Kawamura, K., Kuwano, R., Ono, K., 1996. Neuron–glia interrelations during migration of Purkinje cells in the mouse embryonic cerebellum. Int. J. Dev. Neurosci. 14, 429–438.

Neuroscience Letters 510 (2012) 67–72

Contents lists available at SciVerse ScienceDirect

Neuroscience Letters

journal homepage: www.elsevier.com/locate/neulet

Heparan sulfate niche for cell proliferation in the adult brain

Frederic Mercier[a,*], Eri Arikawa-Hirasawa[b]

[a] Department of Tropical Medicine, Medical Microbiology and Pharmacology, John A. Burns School of Medicine, University of Hawaii, Honolulu, USA
[b] Research Institute for Diseases of Old Age, Juntendo University, Faculty of Medicine, Bunkyo-Ku, Tokyo, Japan

ARTICLE INFO

Article history:
Received 15 September 2011
Received in revised form
22 December 2011
Accepted 22 December 2011

Keywords:
Fractones
Heparan sulfate proteoglycans
Meninges
Mitosis
Neurogenesis
Stem cell niche

ABSTRACT

In adulthood, new neurons and glial cells are generated from stem cells in restricted zones of the brain, namely the olfactory bulb (OB), rostral migratory stream (RMS), subventricular zone (SVZ) of the lateral ventricle, sub-callosum zone (SCZ) and sub-granular layer (SGL) of the dentate gyrus. What makes these zones germinal? We previously reported that N-sulfated heparan sulfates (N-sulfated HS) present in specialized extracellular matrix structures (fractones) and vascular basement membranes bind the neurogenic factor FGF-2 (fibroblast growth factor-2) next to stem cells in the anterior SVZ of the lateral ventricle, the most neurogenic zone in adulthood. To determine to which extent cell proliferation is associated with N-sulfated HS, we mapped N-sulfated HS and proliferating cells by immunohistochemistry throughout the adult mouse brain. We found that cell proliferation is associated with N-sulfated HS in the OB, RMS, the whole germinal SVZ, and the SCZ. Cell proliferation was weakly associated with N-sulfated HS in the SGL, but the SGL was directly connected to a sub-cortical N-sulfated HS+ extension of the meninges. The NS-sulfated HS+ structures were blood vessels in the OB, RMS and SCZ, and primarily fractones in the SVZ. N-sulfated HS+ fractones, blood vessels and meninges formed a continuum that coursed along the OB, SVZ, RMS, SCZ and SGL, challenging the view that these structures are independent germinal entities. These results support the possibility that a single anatomical system might be globally responsible for mitogenesis and ultimately the production of new neurons and glial cells in the adult brain.

The production of new neurons and glia persists throughout adulthood in restricted brain locations termed niches. The niche cells comprise stem cells, progenitor cells, ependymocytes [9] and macrophages [17]. The stem and progenitor cells respond to numerous growth factors and cytokines in a regulating environment that comprise locally produced cell adhesion molecules [4,14,21,22] and extracellular matrix (ECM) molecules [11,19]. The growth factors, which promote stem and progenitor cell proliferation and differentiation, circulate through the brain via the cerebrospinal fluid and eventually reach the neurogenic niche [12]. In the other hand, the ECM and cell adhesion molecules are fixed at the cell surface or in basement membranes, potentially forming the specific niche structures that can capture and promote growth factors to ultimately coordinate stem cell proliferation and differentiation [6,10–12,14,19]. To date, the physiological interactions between ECM, cell adhesion molecules and growth factors in the stem cell niches have not been elucidated. What are the specific ECM or cell adhesion molecules in the neural stem cell niches? Previous publications report that adult neurogenic zones are associated with the polysialylated form of neural cell adhesion molecule (PSA-NCAM) [1,4,5,21,22,24]. PSA-NCAM has been found in the olfactory bulb (OB), subventricular zone (SVZ) of the lateral ventricle, rostral migratory stream (RMS) and sub-granular layer (SGL) of the hippocampus, all neurogenic/gliogenic zones [8,9,13,23] and in sub-pial locations. We have previously shown that proliferating cells in the SVZ of the lateral ventricle are associated with N-sulfated heparan sulfate (N-sulfated HS) proteoglycans [12]. HSPG are highly heterogenous ECM molecules composed of sulfated HS chains attached to a core protein, such as perlecan [2,3]. Numerous growth factors and cytokines, including those promoting stem cell proliferation and differentiation, are heparin-binding molecules [19]. This implies that the growth factor binding to the HS chains of HSPG in the extracellular space is required for growth factor activity [3,6,10,19,20,25]. For, example, fibroblast growth factor-2 (FGF-2) must bind perlecan to promote mitosis in multiple organs and tissues [3,6,25]. It is believed that the pattern of sulfation (N-, O-6, O-3- or O-2-linked) in the glycosylated chains of HSPG is determinant for the selective recognition of growth factors/cytokines [11,19]. We found that N-sulfated HS of the SVZ germinal niche

* Corresponding author at: Department of Tropical Medicine, Medical Microbiology and Pharmacology, John A. Burns School of Medicine, Biomed T401, 1960 East-West Rd, University of Hawaii, Honolulu, HI 96822, USA. Tel.: +1 808 956 7414; fax: +1 808 692 1980.
E-mail address: fmercier@pbrc.hawaii.edu (F. Mercier).

0304-3940/$ – see front matter © 2012 Elsevier Ireland Ltd. All rights reserved.
doi:10.1016/j.neulet.2011.12.046

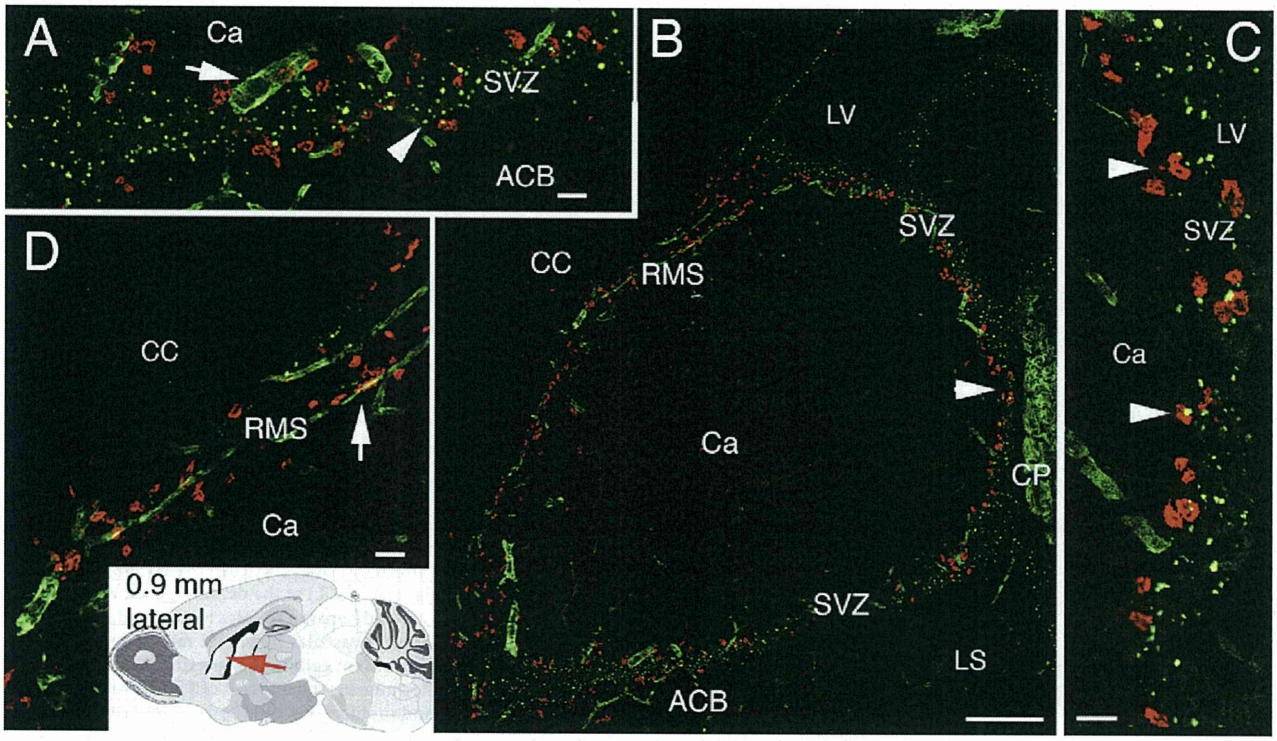

Fig. 1. Cell proliferation is associated with N-sulfated HS in vascular walls, fractone and hybrid vascular/fractone niches. (A) Dual immunolabeling for BrdU (red) and N-sulfated-HS (green) showing cell proliferation next to N-sulfated HS+ fractones (green puncta, arrowhead) and N-sulfated HS+ blood vessels (arrow) in the subventricular zone (SVZ) of a collapsed portion the lateral ventricle at the nucleus accumbens (ACB) surface. Ca: caudate nucleus. The location of this field is indicated by ACB in image (B). (B) Overview of the Ca surface showing the rostral migratory stream (RMS) junction with the SVZ. Proliferating cells are systematically associated with NS-HS immunoreactivity. CP: choroid plexus; LS: lateral septal nucleus. (C) Area of the SVZ (indicated by an arrowhead in (B)) showing cell proliferation associated with N-sulfated HS+ fractones (arrowheads). (D) Magnification of the RMS showing cell proliferation associated with N-sulfated HS+ blood vessels (arrow). The location of all images is shown in the inset. Scale bars. 25 μm in (A, C and D); 200 μm in (B). (For interpretation of the references to color in this figure legend, the reader is referred to the web version of this article.)

were located in the specialized ECM of the SVZ (fractones, [17,18]) and in the walls of SVZ blood vessels. In addition, N-sulfated HS were responsible for the binding of FGF-2 [12].

In the current study, we sought to determine whether N-sulfated HS are expressed in other germinal zones of the adult brain. We used immunofluorescence histochemistry (IHC) to map proliferating cells and N-sulfated HS throughout the brain in serial sections in the adult mouse.

10–20 week old male and female C57/balb C inbred mice ($n = 10$) were used in this study. The animal experimental protocol followed NIH guidelines and was approved by the Institutional Animal Care and Use Committee at the University of Hawaii. The dissected brains were frozen in isopentane at −80 °C, and series of 25-μm-thick coronal and sagittal sections generated with a Leica CM1900 cryostat (Leica Microsystems Buffalo Grove, IL). Individual sections were identified according to bregma or lateral to midline coordinates. Analysis of the distribution of proliferating cells was assessed by IHC for the thymidine analog boromoeoxyuridine (BrdU) on mice that were terminated 5 h after BrdU intraperitoneal injection (50 μg/kg of body weight). Under these experimental conditions, most immunolabeled cells are in S phase. Therefore, immunolabeling for BrdU reflects the distribution of mitogenesis (mitosis initiation). Bisbenzidine "Hoechst 33258" (2 μg/ml, Sigma–Aldrich, Saint Louis, MO) was used to stain cell nuclei. Dual or triple IHC for BrdU (1/500, OBT 0030, Serotec) and the ECM molecules laminin (L9393, 1/1,000, Sigma–Aldrich) and N-sulfated HSPG (antibody 10E4, 1/500, Seikagaku, Japan) was performed as previously described [12]. These primary antibodies were visualized with Alexa-Fluor 546 goat anti-rat, Alexa-Fluor 647 donkey anti-rabbit, and Alexa-Fluor 488 goat anti-mouse IgM (Molecular Probes/Invitrogen, Carlsbad, CA) respectively. Laminin IHC served as a landmark for basement membranes [12,15–18] in the meninges, choroid plexus, blood vessels and fractones (Figs. 2 and 4) [17,18], which appear as puncta (1–6 μm in diameter) along the ventricle walls (Fig. 2C and D). The antibody 10E4, which is specifically directed against N-sulfate glycosamines [7], labeled fractones and meninges but not the majority of blood vessels (Fig. 2); see also [12]. Perlecan (mAb 1948; clone A7 L6; Millipore, Billerica, MA) visualized with AlexaFluor 546 goat anti-mouse was used as an alternative to laminin to visualize blood vessels, fractones and meningeal basement membranes [12]. The images were recorded with 10× and 20× PlanApo dry objectives using a Leica DFC350FX digital camera mounted on a DMIL epifluorescence microscope (Leica Microsystems, Bannockburn, USA), or a Zeiss Confocal LSM510 microscope. The images were processed and mounted as *X–Y* montages (for Figs. 1B, 2B, 3A, 4B, D and E) with Adobe Photoshop CS3 (Adobe Systems, Mountain View, CA). Adjustments for brightness and contrast were minimal.

Fig. 1 shows immunolabeling for proliferating cells (BrdU) and N-sulfated HS at the SVZ/RMS junction. At this location (0.9 mm from the midline), the head of the caudate nucleus fills the cavity of the anterior lateral ventricle, creating two collapsed recesses forming the SVZ/RMS junction (Fig. 1B and schema in D). Each recess consists of two facing ventricle walls containing fractones (green puncta immunoreactive for N-sulfated HS), blood vessels (green tubes) and proliferating cells (BrdU, red) (Fig. 1). The SVZ overlying the caudate is a fractones niche (Fig. 1B and C, arrowheads). The RMS, which does not display fractones, is a vascular niche for

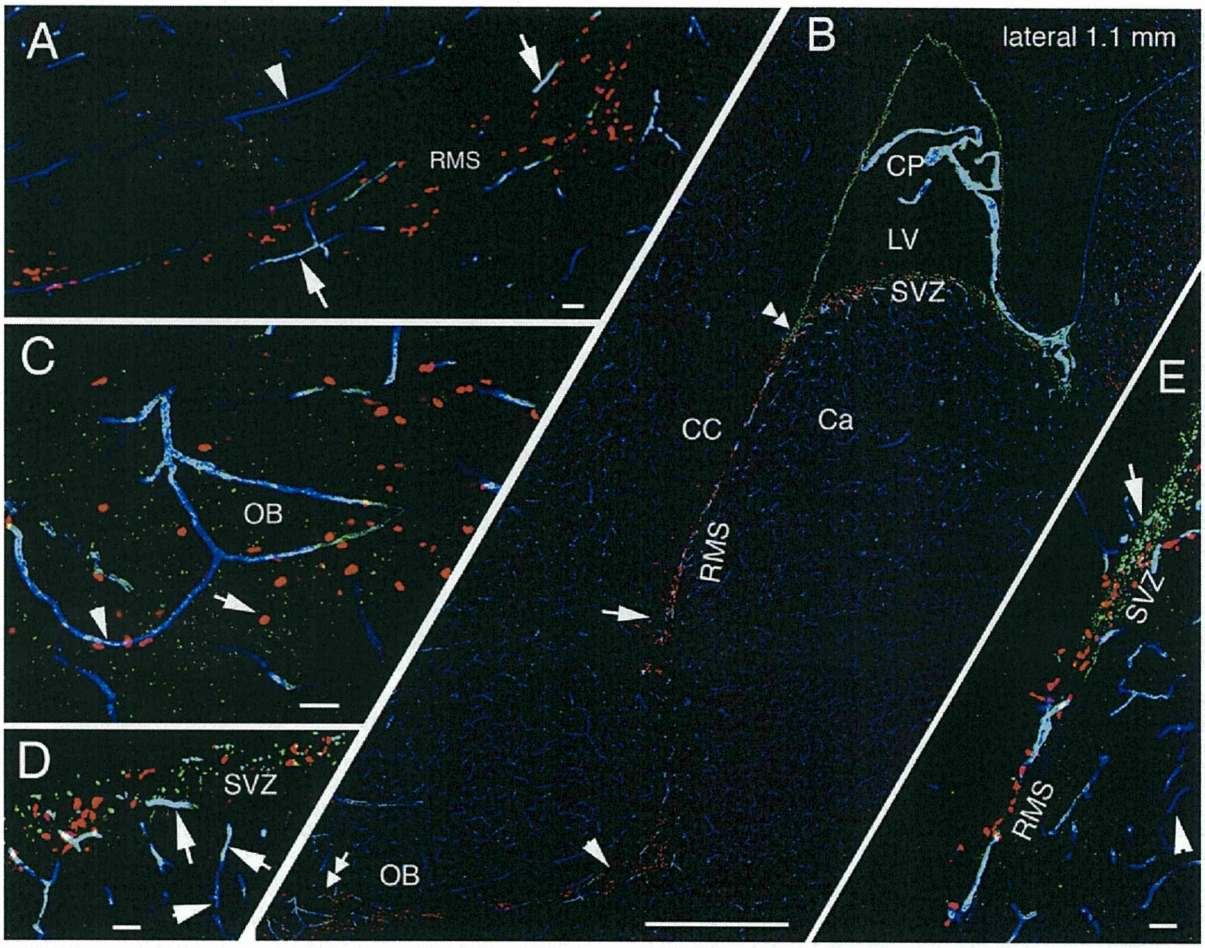

Fig. 2. Cell proliferation is associated with N-sulfated HS in the olfactory bulb and rostral migratory stream. All images display triple immunolabeling for proliferating cells (BrdU, red), N-sulfated HS (green) and laminin (blue) in a sagittal section, 1.1 mm lateral from the midline. Structures that are both laminin+ and N-sulfated HS+ appear turquoise. (A) Magnified field of the zone indicated by an arrowhead in image (B) showing the association of proliferating cells with NS-HS+ blood vessels in the RMS (arrows). Blood vessels away from the RMS are not significantly N-sulfated HS+ and are visualized blue (arrowhead). (B) Overview of the N-sulfated HS niche for cell proliferation showing the OB, RMS and SVZ. CC: corpus callosum; Ca: caudate nucleus; CP: choroid plexus. (C) Magnification of the zone indicated by a double arrow in image (B). Proliferating cells are associated with N-sulfated HS+ puncta < 2 μm in diameter (arrow) and with NS-HS+ blood vessels (arrowhead) in the OB germinal zone. (D) SVZ blood vessels are N-sulfated HS+ and laminin+ (turquoise color, arrow). Blood vessels located beyond the SVZ are laminin+ but do not show significant levels of NS-HS+ (arrowhead). (E) Magnification of the zone indicated by a double arrowhead in image (B). N-sulfated HS niche in the SVZ/RMS junction, showing numerous N-sulfated HS+ fractones (arrow). Beyond the niche, blood vessels do not show significant N-sulfated HS+. Scale bars: 50 μm in (A, C–E); 1 mm in (B). (For interpretation of the references to color in this figure legend, the reader is referred to the web version of this article.)

cell proliferation (Fig. 1D). The antero-ventral portion of the SVZ is a hybrid niche for cell proliferation, consisting of both fractones and N-sulfated HS immunoreactive (N-sulfated HS+) blood vessels (Fig. 1A). In all these zones, no cells initiated proliferation beyond the N-sulfated HS niche (Fig. 1B).

The OB, RMS and SVZ germinal zones can be visualized in a single plane of section at 1.1 mm lateral from the midline (Fig. 2B). Fig. 2 shows triple immunolabeling for BrdU (red), N-sulfated HS (green) and laminin (blue). Structures that contain both laminin and N-sulfated HS appear of turquoise color. A continuum of proliferating cells is associated with N-sulfated HS immunoreactivity from OB to SVZ via the RMS (Fig. 2B). Details of the RMS, OB and SVZ are provided in Fig. 2A, C and E. Unique in the OB germinal zone, proliferating cells were associated with N-sulfated HS+ blood vessels and N-sulfated HS+ puncta showing a diameter < 2 μm (Fig. 2C). An olfactory ventricle no longer exists in the adult mouse, but the distribution of N-sulfated HS+ puncta and proliferating cells correlates with the location of the former SVZ. Similarly, the RMS (Fig. 2A) anatomically corresponds to the embryonic/postnatal aqueduct linking the lateral and olfactory ventricles. This aqueduct no longer exists in adulthood but a N-sulfated HS+ vascular niche for cell proliferation is found throughout the RMS. Again, no proliferating cells were observed beyond the OB/RMS/SVZ axis. This strongly supports the view that mitogenesis occurs along the N-sulfated HS+ niche only (Fig. 2). Blood vessels beyond the germinal niche displayed laminin only (Fig. 2A, arrowhead) whereas those within the germinal niche were immunoreactive for both laminin and N-sulfated HS (Fig. 2A, arrow). Fractones were highly N-sulfated HS+ and appeared green or on a range of colors from green to turquoise, depending on the N-sulfated HS/laminin ratio (Fig. 2E, shown at the RMS/SVZ junction).

Proliferating cells were located in a N-sulfated HS+ niche up to the most lateral portions of the SVZ germinal niche (4 mm to the midline) and are illustrated here at 1.4 mm (Fig. 3D) and 2 mm from the midline (Fig. 3A). This germinal zone corresponds to the SVZ covering the tail of the caudate nucleus, which ultimately reaches the amygdala. In this zone, cells proliferate in a fractone niche (Fig. 3A, arrows), although some N-sulfated HS+

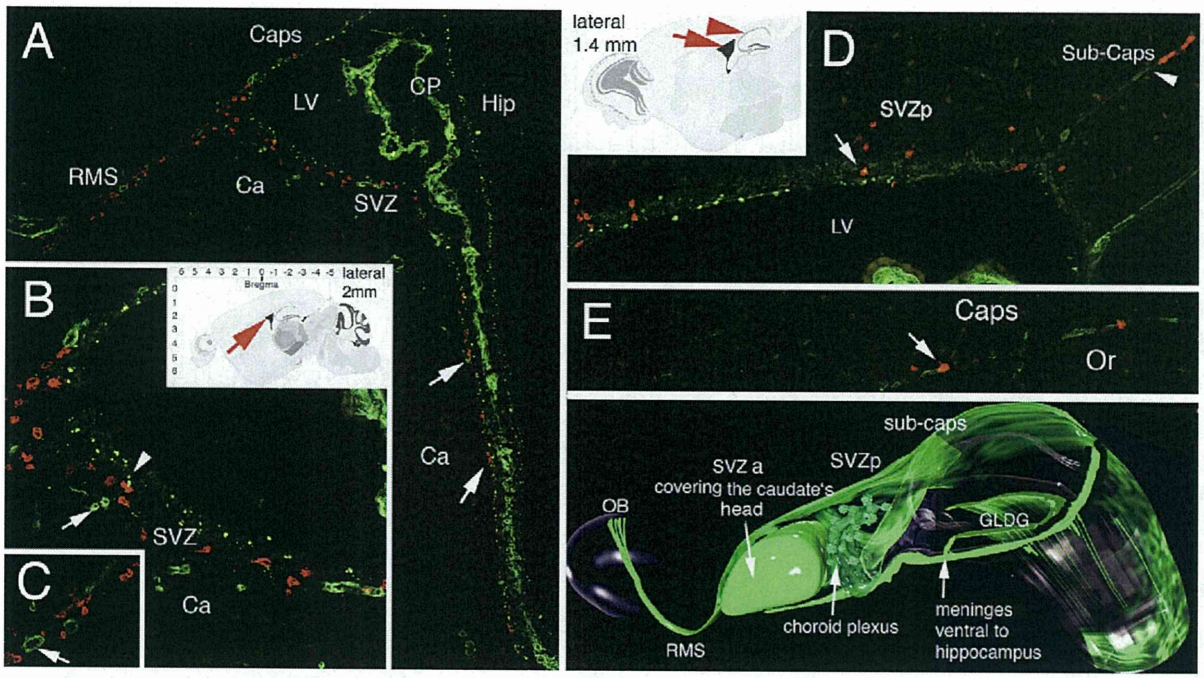

Fig. 3. Cell proliferation is associated with N-sulfated HS throughout the SVZ of the lateral ventricle, sub-callosum and sub-capsule zones. (A) Fractone N-sulfated HS niche for cell proliferation in the lateral portions of the lateral ventricle (LV) wall (2 mm from the midline). Proliferating cells (BrdU+, red) are located in the SVZ next to N-sulfated HS+ (green) fractones (arrows). Ca: caudate nucleus; CP: choroid plexus; Caps: capsule; Hip: hippocampus. (B) Magnified field of the SVZ at the Ca surface showing proliferating cells located between fractones (arrowheads) and capillaries (arrow). The inset indicates the location of images (A–C). (C) In the pathway (horn) leading to the RMS, cells proliferate next to N-sulfated HS+ blood vessels (arrow). (D) Cell proliferation is associated with N-sulfated HS in posterior portions of the SVZ (SVZp). Arrow and arrowhead indicate (D and E) locations, respectively. (E) Cell proliferation is associated with N-sulfated HS+ blood vessels (arrow) between the capsule and the hippocampal Oriens layer (Or). (F) Schematic representation of the N-sulfated HS+ germinal niche, showing all zones illustrated in Figs. 1–3. Scale bars: 100 μm in (A); 50 μm in (B, D and E); 25 μm in (C). (For interpretation of the references to color in this figure legend, the reader is referred to the web version of this article.)

blood vessels were detected. In vascularized zones, proliferating cells were "sandwiched" in between N-sulfated HS+ fractones and blood vessels (Fig. 3B). At 2 mm from the midline, the RMS/SVZ junction is still visible (Fig. 3A and C). Fig. 3D shows the germinal region located underneath the capsule (white matter lateral to the corpus callosum). In this germinal region, first identified by Seri et al. [23] proliferating cells were dispersed and located in an N-sulfated HS+ niche, which contains N-sulfated HS+ fractones where facing the lateral ventricle (Fig. 3D, arrow) but consists of N-sulfated HS+ blood vessels where the capsule (or the corpus callosum) covers the Oriens layer of the hippocampus (Fig. 3D, arrowhead). Fig. 3E shows associations of proliferating cells with the N-sulfated HS+ vascular niche in more posterior portions of the Oriens layer.

To determine whether proliferating cells of the dentate gyrus SGL are associated with a N-sulfated HS niche, we observed series of sections containing the hippocampus. Fig. 4C shows proliferating cells (green) in the SGL at the surface of the compacted neurons forming the GLDG. Only traces of N-sulfated HS immunoreactivity were detected next to the proliferating cells in the SGL (Fig. 4C). Therefore, in contrast to the majority of proliferating cells in the brain (SV, OB, RMS and SCZ), cell proliferation in the SGL does not evidently occur in an N-sulfated HS+ niche. To determine whether expression of heparan sulfates in the SGL depends of the age of the animal, we compared 5-week, 10-week and 20-week old mice for the expression of N-sulfated HS in the SGL. Figures G–I show that only traces of N-sulfated HS can be seen in the vasculature supplying the SGL at all these ages. However, a N-sulfated HS+ meningeal extension coursing ventral to the hippocampus connects the GLDG/SGL (Fig. 4A and C, bottom arrow). An overview of the dentate gyrus and its connection to the meninge, detected by laminin immunoreactivity, is shown in Fig. 4A. The SGL/meninge connection site often displayed proliferating cells (Fig. 4C, arrow). Fig. 4D and E shows the course of the N-sulfated HS+ meningeal extension within the brain and its relation with the superficial ventral meninges near the posterior communicans artery (circle of Willis, arrowhead). Fig. 4B shows the course of this N-sulfated HS+ meninge from the choroid plexus of the lateral ventricle (arrow) towards the dorsal brain, connecting 'en route' the SGL (asterisk). The anatomy of the meninges within the brain and their relationships with the superficial meninges are schematized in Fig. 4E, inset.

In conclusion, we found that mitogenesis is remarkably associated with a N-sulftated HS niche. This niche courses as a single anatomical system in the OB, RMS, SVZ and SCZ/sub-capsule (junction zones shown in Figs. 1–3) and appears to be continuous with N-sulfated HS+ sub-cortical meninges connecting the hippocampal neurogenic zone (Fig. 4B). The N-sulfated HS niche comprises fractones and blood vessel walls (Figs. 1–3), although the exact nature of the N-sulfated HS niche structures within the blood vessel walls has not been yet identified. We show a schematic representation of the germinal system of the adult brain (Fig. 4F, red) and its anatomical relationship with the meninges (Fig. 4F, yellow). The N-sulfated HS niche for mitogenesis forms a unique anatomical system, which is reminiscent, although not identical, to the PSA-NCAM niche previously identified in neurogenic zones [1,4,5,21,22,24]. A difference between the pattern of PSA-NCAM and N-sulfated HS is the subpial (from the former) versus the pial location (for the latter). Since HS are responsible for growth factor binding and activation at the surface of target cells [3,10,25] the current results suggest the existence of a functional system involved in the regulation of growth factors in the brain germinal zones.

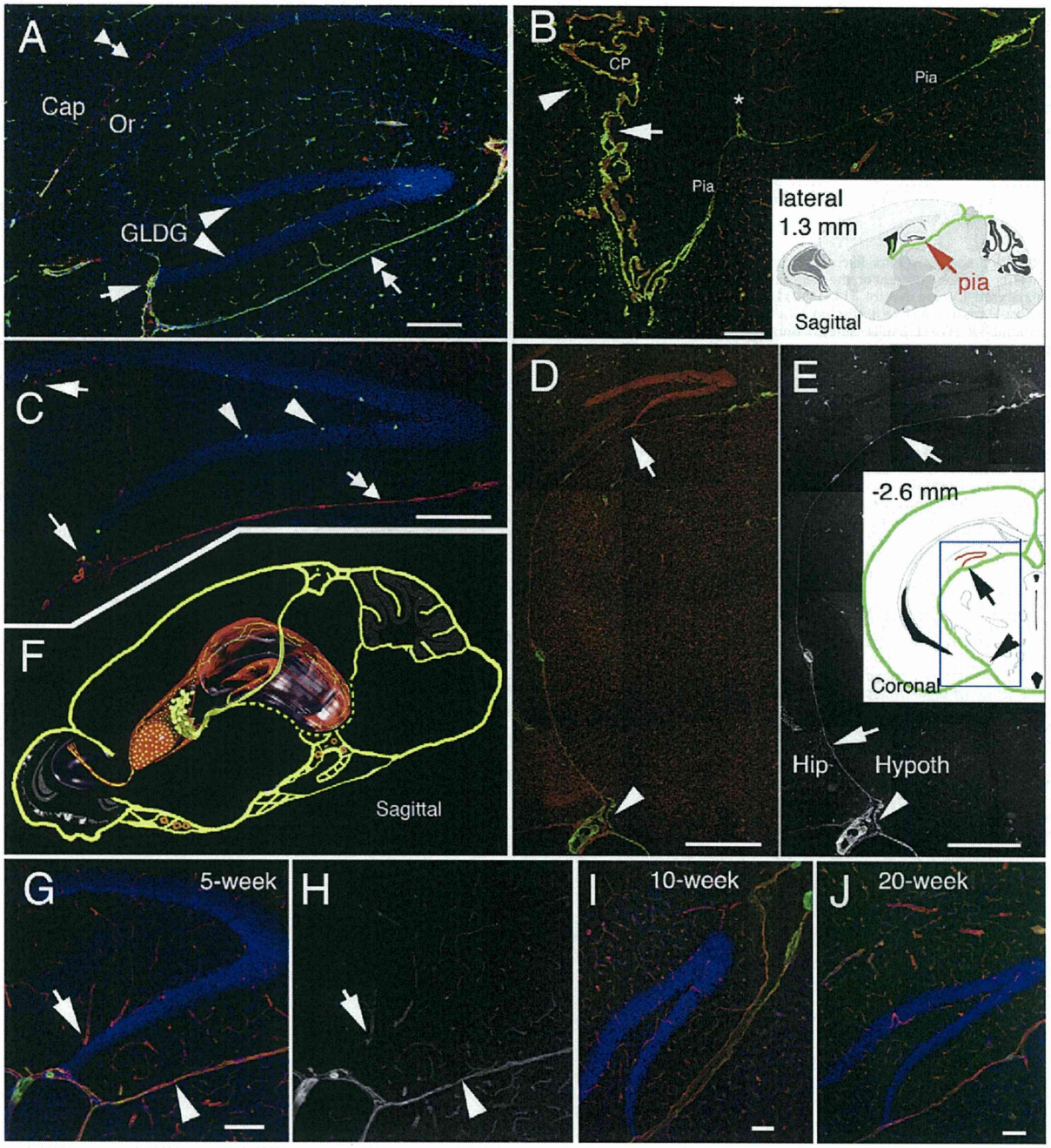

Fig. 4. Cell proliferation in the dentate gyrus sub-granular layer (SGL) is not associated with N-sulfated HS but is connected to N-sulfated HS+ meninges. (A) Sagittal section labeled for laminin (green), NS-HS (red) and bisbenzidine (blue) showing the granular layer of the dentate gyrus (GLDG), visualized by high neuronal nuclear density (arrowheads). The GLDG connects a meningeal extension, visualized by laminin+ basement membranes, coursing ventral to the hippocampus (double arrow). The N-sulfated HS+ niche of the sub-capsule (double arrowhead) is visible in between the hippocampal Oriens layer (Or) and the capsule (Cap). (B) Immunolabeling for perlecan (red) and N-sulfated HS (green) showing fractones (arrowhead) and the meningeal trajectory from the choroid plexus (CP, arrow) of the lateral ventricle to the dorsal cortex. The CP displays a mixed pattern of N-sulfated HS and laminin (arrow). The asterisk shows the GLDG/meningeal connection. (C) Most proliferating cells (BrdU+, green) in the SGL (located beneath the GLDG) are not associated with N-sulfated HS+ (arrowheads). Some are (arrows), primarily next to the N-sulfated HS+ meninge (bottom arrow). This meningeal extension courses beneath the hippocampus (double arrow). (D and E) Coronal sections showing the connection (arrow) of the GLDG (bisbenzidine+, red) with the N-sulfated HS+ meninge (green). Arrowhead: arteries of the circle of Willis at the brain surface. The N-sulfated HS+ meninges (shown without bisbenzidine in (E)) separate sub-cortical from hypothalamic/thalamic structures (arrows). The location of images (D and E) is indicated in the inset (blue frame). The trajectory of the meninges is shown in green. (F) Schematic sagittal representation of the meninges (yellow) and germinal zones (red). Dashed lines indicate trajectories beyond the plane of section. (G) SGL of a 5-week old mouse showing cell nucleus labeling (blue), laminin (red) and N-sulfated-HS (green). (H) Same as G displaying N-sulfated-HS only. Only traces of N-sulfated-HS are present in the SGL vasculature (arrow). Most labeling is located in the meninge ventral to the hippocampus (arrowhead). (I and J) Similar locations in 10- and 20-week old mice showing no significant N-sulfated-HS in the SGL. Scale bars. 200 μm in (A–C); 500 μm in (D and E); 100 μm in (G–J). (For interpretation of the references to color in this figure legend, the reader is referred to the web version of this article.)

Acknowledgments

We thank Dr. Aurelien Kerever for designing the three-dimensional schematic representation of mitogenesis in the adult brain, using the 3D-computer graphic software Blender (Netherlands). This work was supported by NIH RRNIH R21 NS057675-01, RCMI 5G12/A103061 and Japanese Society for the Promotion of Science S09109.

References

[1] G. Alonso, Neuronal progenitor-like cells expressing polysialylated neural cell adhesion molecule are present on the ventricular surface of the adult rat brain and spinal cord, J. Comp. Neurol. 414 (1999) 149–166.
[2] E. Arikawa-Hirasawa, A.H. Le, I. Nishino, I. Nonaka, N.C. Ho, C.A. Francomano, P. Govindraj, J.R. Hassel, J.M. Devaney, J. Spranger, R.E. Stevenson, S. Lannacoonie, M.C. Dalakas, Y. Yamada, Structural and functional mutations of the perlecan gene cause Schwartz-jampel syndrome, with mitotic myopathy and chondrodysplasia, Am. J. Hum. Genet. 70 (2002) 1368–1375.
[3] D. Aviezer, D. Hecht, M. Safran, M. Elsinger, G. David, A. Yayon, Perlecan, basal lamina proteoglycan, promotes basic fibroblast growth factor-receptor binding, mitogenesis and angiogenesis, Cell 79 (1994) 1005–1013.
[4] L. Bonfanti, PSA-NCAM in mammalian structural plasticity and neurogenesis, Prog. Neurobiol. 80 (2006) 129–164.
[5] L. Bonfanti, D.T. Theodosis, Expression of polysialylated neural cell adhesion molecule by proliferating cells in the subependymal layer of the adult rat, in its extension and in the olfactory bulb, Neuroscience 62 (1994) 291–305.
[6] Y.G. Brickman, M.D. Ford, D.H. Small, P.F. Bartlett, V. Nurcombe, Heparan sulfates mediate the binding of basic fibroblast growth factor to a specific receptor on neural precursor cells, J. Biol. Chem. 270 (1995) 24941–24948.
[7] G. David, X. Mei Bai, B. Van Der Schueren, J.J. Cassiman, H. Van Den Berghe, Developmental changes in heparan sulfate expression: in situ detection with mAbs, J. Cell Biol. 119 (1992) 961–975.
[8] G.D. Das, J.J. Altman, Postnatal neurogenesis in the caudate nucleus an nucleus accumbens septi in the rat, Brain Res. 21 (1970) 122–127.
[9] F. Doetsch, J.M. Garcia-verdugo, A. Alvarez-Buylla, Cellular composition and three-dimensional organization of the subventricular germinal zone in the adult mammalian brain, J. Neurosci. 17 (1997) 5046–5061.
[10] C. Dombrowski, S.J. Song, P. Chuan, X.H. Lim, E. Susanto, A.A. Sawyer, M.A. Woodruff, D.W. Hutmacher, V. Nurcombe, S.M. Cool, Heparan sulfate mediates the proliferation and differentiation of rat mesenchymal stem cells, Stem Cells Dev. 18 (2009).
[11] P. Gupta, T.R. Oegema Jr., J.J. Brazil, A.Z. Dudek, A. Slungaard, C.M. Verfaillie, Structurally specific heparan sulfates support primitive human hematopoeisis by formation of a multimolecular stem cell niche, Blood 92 (1998) 4641–4651.
[12] A. Kerever, J. Schnack, D. Vellinga, N. Ichikawa, C. Moon, E. Arikawa-Hirasawa, J.T. Efird, F. Mercier, Novel extracellular matrix structures in the neural stem cell niche capture the neurogenic factor FGF-2 from the extracellular milieu, Stem Cells 25 (2007) 2146–2157.
[13] C. Lois, A. Alvarez-Buylla., Proliferating subventricular zone cells in the adult mammalian forebrain can differentiate into neurons and glia, Proc. Natl. Acad. Sci. 90 (1993) 2074–2077.
[14] V. Marthiens, I. Kazanis, L. Moss, K. Long, C. Ffrench-Constant, Adhesion molecules in the stem cell niche – more than just staying in shape? J. Cell Sci. 123 (2010) 1613–1622.
[15] F. Mercier, G.I. Hatton, Meninges and perivasculature as mediators of CNS plasticity, in: E.E. Bittar, L. Hertz (Eds.), Non-Neuronal Cells in the Nervous System: Function and Dysfunction, Elsevier Bioscience, Amsterdam, Advances Mol. Cell Biol. 31 (2004) 215–253.
[16] F. Mercier, G.I. Hatton, Connexin 26 and basic fibroblast growth factor are expressed primarily in the sub-pial and subependymal layers in adult brain parenchyma: Roles in stem cell proliferation and morphological plasticity? J. Comp. Neurol. 431 (2001) 88–104.
[17] F. Mercier, J.T. Kitasako, G.I. Hatton, Anatomy of the brain neurogenic zones revisited: fractones and the fibroblast/macrophage network, J. Comp. Neurol. 451 (2002) 170–188.
[18] F. Mercier, J.T. Kitasako, G.I. Hatton, Fractones and other basal laminae in the hypothalamus, J. Comp. Neurol. 455 (2003) 324–340.
[19] F. Mercier, J. Shnack, M. Saint Georges Chaumet, Fractones: home and conductors of the neural stem cell niche, in: A. Alvarez-Buylla, J.M. Parent, K. Sawamoto, T. Seki (Eds.), Neurogenesis in the Adult Brain, Springer Verlag Pub., 2011 (Chapter 4).
[20] R. Roberts, J. Ghallager, E. Spooncer, T.D. Allen, F. Bloomfield, T.M. Dexter, Heparan-sulfate bound growth factors: a mechanism for stromal cell mediated hematopoesis, Nature 332 (1988) 376–378.
[21] T. Seki, Hippocampal adult neurogenesis occurs in a microenvironment provided by PSA-NCAM-expressing immature neurons, J. Neurosci. Res. 69 (2002) 772–783.
[22] T. Seki, Y. Arai, Distribution and possible role of the high polysialylated neural cell adhesion molecule (NCAM-H) in the developing and adult central nervous system, Neurosci. Res. 17 (1993) 265–290.
[23] B. Seri, D.G. Herrera, A. Gritti, A. Ferron, L. Collado, J.M Garcia Verdugo, A. Alvarez-Buylla, Composiiton and organization of the SCZ: a large germinal layer containing cotaining neural stem cells in the adult mammalian brain, Cereb. Cortex 16 Suppl. 1 (2006) i103–i116.
[24] D.T. Theodosis, G. Rougon, D.A. Poulain, Retention of embryonic features by an adult neuronal system capable of plasticity: polysialylated neural cell adhesion molecule in the hypothalamo-neurohypophysial system, Proc. Natl. Acad. Sci. 88 (1991) 5494–5498.
[25] A. Yayon, M. Klagsbrun, J.D. Esko, P. Leder, D.P. Ornitz, Cell surface heparin-like molecules are required for binding of fibroblast growth factor to its high affinity receptor, Cell 64 (1991) 841–848.

SCIENTIFIC REPORTS

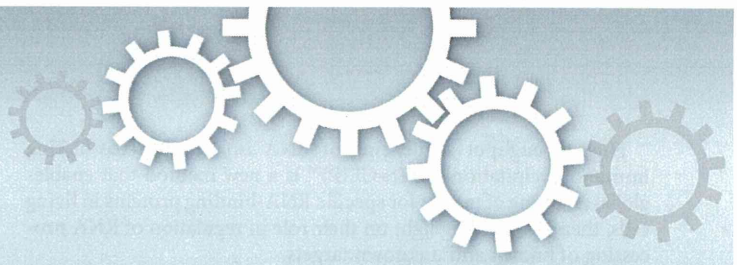

OPEN

SUBJECT AREAS:
CELLULAR NEUROSCIENCE
MOTOR SYSTEM
GENE REGULATION
TRANSCRIPTOME

Received
25 August 2011

Accepted
8 December 2011

Published
4 January 2012

Correspondence and requests for materials should be addressed to K.O. (ohnok@med.nagoya-u.ac.jp)

*These authors contributed equally to this work.

CUGBP1 and MBNL1 preferentially bind to 3′ UTRs and facilitate mRNA decay

Akio Masuda[1], Henriette Skovgaard Andersen[2]*, Thomas Koed Doktor[2]*, Takaaki Okamoto[1], Mikako Ito[1], Brage Storstein Andresen[2] & Kinji Ohno[1]

[1]Division of Neurogenetics, Center for Neurological Diseases and Cancer, Nagoya University Graduate School of Medicine, Nagoya, Japan, [2]Department of Biochemistry and Molecular Biology, University of Southern Denmark, Odense M, Denmark.

CUGBP1 and MBNL1 are developmentally regulated RNA-binding proteins that are causally associated with myotonic dystrophy type 1. We globally determined the *in vivo* RNA-binding sites of CUGBP1 and MBNL1. Interestingly, CUGBP1 and MBNL1 are both preferentially bound to 3′ UTRs. Analysis of CUGBP1- and MBNL1-bound 3′ UTRs demonstrated that both factors mediate accelerated mRNA decay and temporal profiles of expression arrays supported this. Role of CUGBP1 on accelerated mRNA decay has been previously reported, but the similar function of MBNL1 has not been reported to date. It is well established that CUGBP1 and MBNL1 regulate alternative splicing. Screening by exon array and validation by RT-PCR revealed position dependence of CUGBP1- and MBNL1-binding sites on the resulting alternative splicing pattern. This study suggests that regulation of CUGBP1 and MBNL1 is essential for accurate control of destabilization of a broad spectrum of mRNAs as well as of alternative splicing events.

In recent years, new technologies, such as microarray analysis and high throughput sequencing, have dramatically changed our knowledge on gene expression and revealed that extensive regulation takes place during posttranscriptional RNA processing[1]. Numerous RNA processing elements and regulatory RNA-binding proteins play together in a finely tuned interplay to ensure that different mRNAs are made from the primary transcript from a gene and are present in the right cell at the right time and in the correct amounts. Such complex regulation is of course vulnerable and a rapidly increasing number of human diseases are now known to be caused by misregulated RNA processing[2]. An intriguing example where this kind of disease mechanism is in operation is myotonic dystrophy type 1 (DM1), where aberrant regulation of two RNA-binding proteins, CUG-binding protein 1 (CUGBP1) and muscleblind-like 1 (MBNL1) co-operationally cause some of the disease symptoms. DM1 is the most common form of myotonic dystrophy (DM), and is caused by an expansion of CTG-repeats in the 3′ untranslated region (UTR) of the DM protein kinase gene (*DMPK*) on chromosome 19[3–5]. DM1 is a multisystemic disorder and the clinical features include myotonia, muscle degeneration, heart failure, ocular cataracts, impaired glucose tolerance, and mental retardation[6,7]. A dominant negative effect of the *DMPK* mutant allele through RNA gain-of-function has been proposed as the molecular disease mechanism. Many studies support a mechanism where toxic *DMPK* RNA with expanded CUG repeats binds to and sequesters proteins that are important for RNA metabolism including transcription, RNA transport, alternative splicing, translation, and yet unknown processes[6]. The expanded CUG repeats in the *DMPK* mRNA bind to and sequestrate MBNL1 in discrete nuclear foci, which results in depletion of functional MBNL1[8,9]. By a yet unknown mechanism the expanded CUG repeats also activate protein kinase C (PKC), which phosphorylates and stabilizes CUGBP1[10]. Thus, the expanded CUG repeats contribute to DM1 pathogenesis by causing loss of MBNL1 and gain of CUGBP1 activity[11].

Both CUGBP1 and MBNL1 regulate postnatal transitions in alternative splicing patterns during striated muscle development[9,12,13]. Representative targets of CUGBP1 splicing regulation, which are misregulated in DM1 striated muscles, include genes for cardiac troponin T (*TNNT2*)[14,15], insulin receptor (*INSR*)[16], and chloride channel 1 (*CLCN1*)[15,17]. MBNL1 contains four CCCH-type zinc fingers that recognize a YGCY motif that is indeed observed in the CUG repeat (CUGCUG)[18–21]. Mice deficient in *Mbnl1* show aberrant splicing of *Clcn1*, *Tnnt2*, and *Tnnt3*, but not *Insr*[22]. Very recently, MBNL1 was shown to regulate *BIN1* alternative splicing, and dysregulation of *BIN1* splicing in DM1 muscles was suggested to be part of the disease pathology resulting in muscle weakness[23]. Besides an important role in splicing regulation, CUGBP1 mediates mRNA decay of short-lived transcripts by interaction with GU-rich elements in the 3′ UTR[24–27]. In addition, CUGBP1 increases the translation of *CDKN1A*[28] and *Mef2a*[29]. In contrast to the multiple functionalities in posttranscriptional gene regulation of CUGBP1, MBNL1 has so far been exclusively recognized as a splicing regulatory *trans*-factor.

High-throughput sequencing of RNA isolated by crosslinking immunoprecipitation (HITS-CLIP)[30] is a new method that enables global mapping of targets for specific RNA-binding proteins in living cells, thereby shedding light on their role in regulation of RNA processing of known and unknown targets.

In the present study, we performed HITS-CLIP analysis for CUGBP1 and MBNL1 on the mouse myoblast cell line C2C12 to extensively characterize their RNA-binding sites and functional roles in RNA processing. We identified position-dependence of CUGBP1/MBNL1-binding sites in regulating exon inclusion or skipping. Interestingly, we discovered that both CUGBP1 and MBNL1 preferentially bind to the 3′ UTR and destabilize target mRNAs. This points to a new important role of MBNL1 and suggests that binding to the 3′ UTRs and destabilization of mRNA are likely to be a fundamental function shared by CUGBP1 and MBNL1.

Results

Genome-wide CUGBP1/MBNL1-RNA interaction maps. In order to determine global CUGBP1/MBNL1-binding sites *in vivo*, we performed HITS-CLIP experiments using the mouse myoblast cell line, C2C12.

In C2C12 cells, CUGBP1 is constantly expressed throughout myoblast differentiation, whereas expression of MBNL1 is low in undifferentiated cells and gradually increases during differentiation (Supplementary Fig. S1), as previously described[8]. We thus performed HITS-CLIP analysis of CUGBP1 and MBNL1 using undifferentiated and differentiated C2C12 cells, respectively. We also performed CLIP of MBNL1 using undifferentiated cells in three independent experiments, but this yielded an insufficient amount of RNA-protein complexes and failed to yield cDNA libraries suitable for high-throughput sequencing. In the HITS-CLIP analysis of CUGBP1, our first experiment yielded 34,733,815 CLIP tags of 32 nt, of which 29,545,067 (85.06%) were mapped to the mm9 genome allowing at most 2 mismatches and placing reads mapping to multiple locations to a single random site. A second CLIP experiment yielded 10,079,185 CLIP tags of 36 nt, of which 8,516,256 (84.49%) were mapped. In the first MBNL1 CLIP experiment, we obtained 13,218,685 CLIP tags, of which 11,044,152 (83.55%) were mapped, while the second CLIP experiment yielded 13,474,600 CLIP tags with 11,455,886 (85.02%) tags mapped to the mm9 genome. For the analysis of binding motif and binding region annotation, we selected only reads that were aligned uniquely in the genome and removed all potential PCR duplicates by collapsing reads with an identical 5′ start into a single read. This resulted in 177,013 and 130,828 CLIP tags from the two CUGBP1 CLIP experiments, while the two MBNL1 experiments yielded 59,156 and 583,841 CLIP tags respectively.

In an effort to confirm the specificity of our CLIP experiments, we performed CLIP analysis of polypyrimidine tract-binding protein (PTB), a multifunctional RNA-binding protein, using undifferentiated mouse C2C12 cells. We identified 12,841,778 CLIP tags of which 11,184,829 (87.10%) were mapped to the mouse mm9 genome. Removal of non-uniquely aligned reads and PCR duplicates yielded 307,995 unambiguous CLIP tags.

Consensus motifs. To determine RNA-binding motifs associated with CUGBP1/MBNL1 *in vivo*, we used the motif-finding algorithm, Multiple EM for Motif Elicitation (MEME)[31]. We used SeqMonk to identify likely binding regions, and identified 1,841 CUGBP1-binding regions and 302 MBNL1-binding regions. Comparison of SeqMonk's maximum depth scores between samples indicates that binding regions in each replicated experiment are highly overlapping, while PTB binding regions did not overlap with those of the other four CLIP experiments (Supplementary Fig. S2). The lower number of identified MBNL1 regions supported by two independent experiments (Supplementary Fig. S2b) was likely due to the large difference in the number of CLIP tags in the two MBNL1 experiments. The regions demonstrate enrichment of GU-rich motifs for CUGBP1 and YGCY-containing motifs for MBNL1 (Fig. 1).

Our *in vivo* binding motifs are in accordance with previously suggested binding motifs for CUGBP1[25,32] and MBNL1[21,33–35]. We identified 1,824 PTB binding regions in the mouse genome and detected a CU-rich motif, which is essentially identical to the motif for PTB recently identified by HITS-CLIP analysis of a human cell line[36].

We also analyzed the CUGBP1 and MBNL1 motifs enriched in regions containing reads with multiple potential mapping locations (Supplementary Fig. S3), and compared them with the motifs with unique mapping (Fig. 1). Following removal of potential PCR duplicates, we observed 699,382 tags that were non-uniquely aligned in the 1st CUGBP1 CLIP experiment, 219,128 tags in the 2nd CUGBP1 CLIP experiment, 105,432 and 216,882 tags in the two MBNL1 CLIP experiments respectively and finally 851,324 tags in the PTB CLIP experiment. We observed that enriched motifs in these regions (Supplementary Fig. S3) are very similar to the CUGBP1 and MBNL1 motifs enriched in the binding regions containing uniquely aligned reads (Fig. 1), suggesting that these regions share the same properties as the uniquely aligned regions and that they may contain functional binding sites.

HITS-CLIP analysis of splicing targets. We next studied the effects of CUGBP1/MBNL1 binding on alternative splicing. CUGBP1 tags are clustered in intronic regions flanking alternative rather than

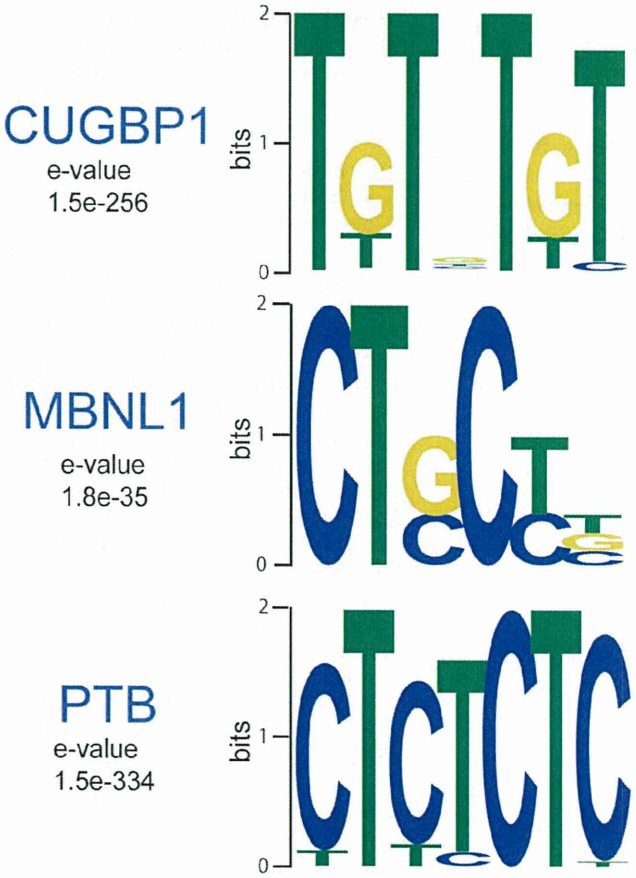

Figure 1 | Binding motif analysis. WebLogos of consensus binding motifs of CUGBP1, MBNL1, and PTB generated by the MEME motif analysis tool. The likelihood of finding the indicated motif by chance is indicated as an E-value.

constitutive exons (Fig. 2a). MBNL1 tags are similarly clustered in intronic regions flanking alternative exons, and are also enriched in alternative and constitutive exons. In order to investigate if and how CUGBP1/MBNL1 binding around splice sites regulate alternative splicing, we knocked down these factors by siRNA in undifferentiated C2C12 cells (Supplementary Fig. S4a). We analyzed alterations of splicing globally using the Affymetrix Mouse Exon 1.0 ST Array (GEO accession number, GSE29990) and identified 8 CUGBP1-responsive and 24 MBNL1-responsive exons (Supplementary Table 1, Figs. S5 and S6abc). We also analyzed 29 CUGBP1-tagged and 51 MBNL1-tagged exons/introns known to be alternatively spliced according to the ENSEMBL version *e!*61, and identified 16 CUGBP1-responsive and 21 MBNL1-responsive exons by RT-PCR (Supplementary Figs. S5 and S6abc). We made the compiled dataset C, which is comprised of the 24 CUGBP1-regulated exons (15 skipped and 9 included), as well as the compiled dataset M consisting of the 45 MBNL1-regulated exons (25 skipped and 20 included). The datasets include 1 and 9 previously identified target exons of CUGBP1 and MBNL1, respectively (Supplementary Fig. S5). In addition, 9 exons are shared between datasets C and M. Mbnl1 siRNA sufficiently suppressed MBNL1 expression up to day 3 after differentiation (Supplementary Fig. S4b), and we observed that as many as 44 of the 45 MBNL1-regulated exons in dataset M respond similarly to MBNL1 knockdown in both differentiated and undifferentiated cells (Supplementary Figs. S4 and S5).

We also made dataset M2 that includes 26 additional MBNL1-dependent cassette exons (15 skipped and 11 included) that were previously identified in skeletal muscle of MBNL1 knockout mice

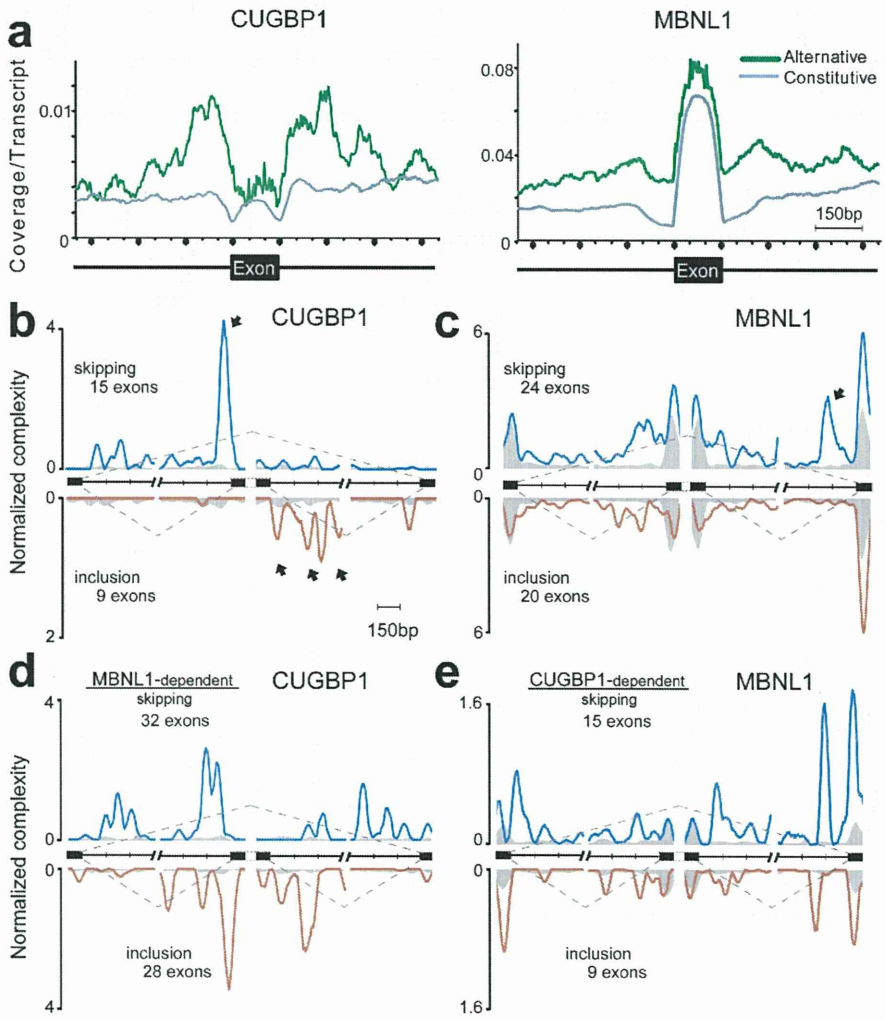

Figure 2 | Mapping of CLIP-tags on exon-intron structures. (a) Distributions of CLIP-tags on constitutively or alternatively spliced exons and the flanking intronic regions. The abscissa indicates an intron-exon-intron structure. The sizes of all the exons are normalized to 150 nucleotides. Numbers of exonic CLIP-tags are also normalized accordingly. Intronic CLIP-tags within 500 nucleotides upstream or downstream of exons are indicated. The number of CLIP-tags is normalized for the number of transcripts belonging to either category of constitutive and alternative exons. (b) Normalized complexity map of CUGBP1 at CUGBP1-dependent splice sites. Twenty-four CUGBP1-regulated splicing events in dataset C in undifferentiated C2C12 cells are compiled. (c) Normalized complexity map of MBNL1 at MBNL1-dependent splice sites. Forty-four MBNL1-regulated splicing events in differentiated C2C12 cells in dataset M are compiled. (d) Normalized complexity map of CUGBP1 at MBNL1-dependent splice sites. Sixty MBNL1-regulated splicing events in undifferentiated C2C12 cells in datasets M and M2 are compiled. (e) Normalized complexity map of MBNL1 at CUGBP1-dependent splice sites. Twenty-four CUGBP1-regulated splicing events in undifferentiated C2C12 cells in dataset C are compiled. Shaded areas represent an average of 100 sets of normalized complexity of 50 (b, c, and d) and 15 (e) randomly selected constitutive exons. Arrows indicate representative peaks that are explained in Results. Graphs represents results of the 2nd CLIP experiments for both CUGBP1 and MBNL1. Resutls of the 1st CLIP experiments are shown in Supplmentary Fig. S7.

(Supplementary Table S2)[33], and found that 18 exons are similarly regulated by *Mbnl1* knockdown in undifferentiated C2C12 cells (Supplementary Fig. S6d and Table S2).

We combined datasets C and M into a single composite pre-mRNA and made integrated RNA maps from our HITS-CLIP reads mapped to the corresponding genomic regions as previously described for Nova[30] and PTB[36]. This showed that CUGBP1 binding to upstream intronic regions facilitates exon skipping, whereas CUGBP1 binding to downstream intronic regions promotes exon inclusion (closed arrows in Fig. 2b and Supplementary Fig. S7a). Results of the 2nd experiments are shown in Fig. 2 and those of the 1st experiments are in Supplementary Fig. S7. In contrast, although the binding sites of MBNL1 are more diffusely distributed and less abundant in regions flanking splice sites (Fig. 2c), MBNL1 binding close to the 3′ end of the downstream intron induces exon skipping (closed arrow in Fig. 2c and Supplementary Fig. S7b). The presence of a similar peak in dataset M2 (closed arrow in Supplementary Fig. S7c) further supports this observation.

We next analyzed the interaction between CUGBP1 and MBNL1 in splicing regulation. We made an RNA map of CUGBP1-binding sites in MBNL1-regulated exons from datasets M and M2 (Fig. 2d and Supplementary Fig. S7e), as well as an RNA map of MBNL1-binding sites in CUGBP1-regulated exons from dataset C (Fig. 2e and Supplementary Fig. S7f). Both RNA maps demonstrate the presence of CUGBP1 clusters in MBNL1-responsive exons and vice versa, which suggests that CUGBP1 and MBNL1 are likely to regulate alternative splicing of some of the same exons.

MBNL1 and CUGBP1 both preferentially bind to the 3′ UTR. MBNL1 has so far solely been categorized as an exon/intron-binding splicing regulatory protein[6], but to our surprise we found that the majority (55%) of MBNL1-binding regions are located in 3′ UTRs (Fig. 3a). The same pattern with preferential binding (53%) in 3′ UTRs is observed for CUGBP1, while only 2% of PTB binding regions are located in 3′ UTRs (Fig. 3a). Similarly, when HITS-CLIP tags are mapped to the size-normalized positions of all the genes in the mouse genome, CUGBP1 and MBNL1 CLIP tags, but not PTB CLIP-tags, are enriched close to the 3′ ends of genes (Fig. 3b). Additionally, 610 3′ UTRs, which constitutes 28.7% of the CUGBP1-tagged 3′ UTRs and 17.4% of the MBNL1-tagged 3′ UTRs, are shared

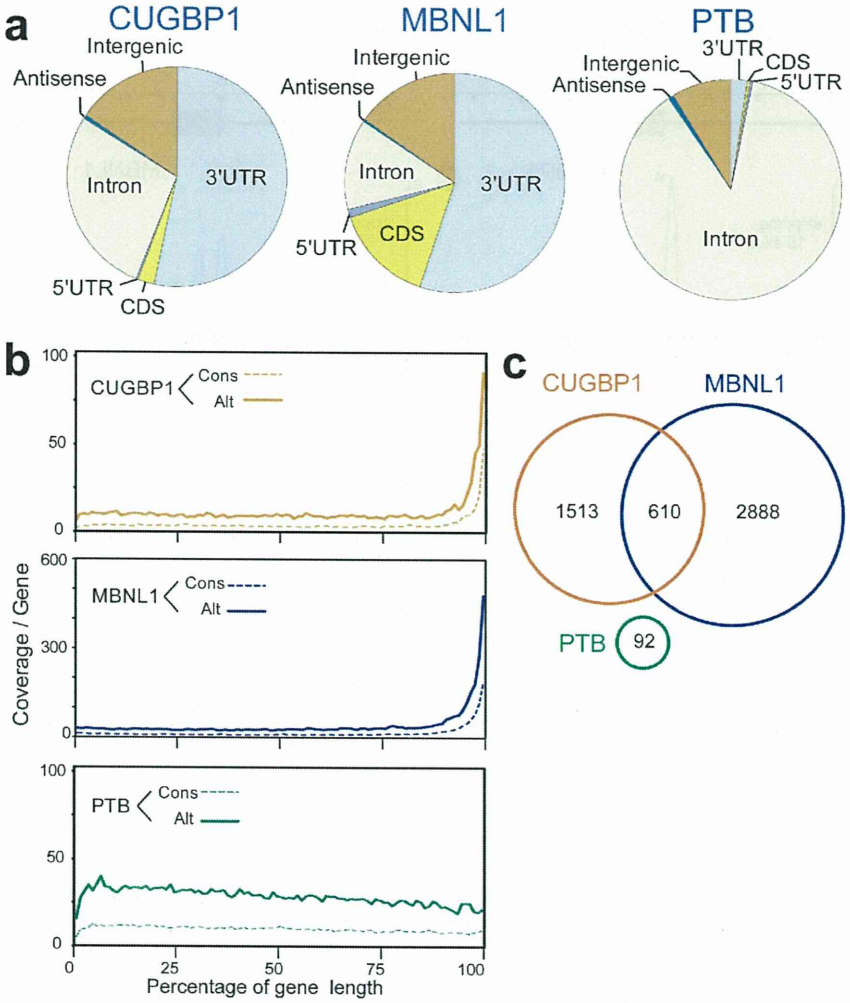

Figure 3 | Enrichment of CUGBP1 and MBNL1 CLIP-tags in the 3′ UTR. (a) Distributions of CUGBP1, MBNL1, and PTB binding regions. Binding regions are mapped to CDS (coding sequence), 5′ and 3′ UTRs, introns, intergenic regions (incl. tRNA and rRNA genes), or antisense within genes according to the UCSC knownGene annotation of the NCBI Build 37.1 mouse genome (mm9). Pie-charts show ratios of binding regions mapped to the indicated regions. (b) Distributions of CUGBP1, MBNL1, and PTB CLIP-tags mapped to the relative positions of all the mouse genes. The relative positions of the genes are shown in percentages of the gene length in abscissa. The broken lines represent 15,638 genes with constitutive transcriptional start and end sites (Cons), and the solid lines represent 7,477 genes with alternative transcriptional start or end site (Alt). (c) Venn diagram of the numbers of genes with CUGBP1-, MBNL1-, and PTB-binding regions within the 3′ UTR. Binding regions were identified using the SeqMonk software.

between these two proteins (Fig. 3c). All these data document that both CUGBP1 and MBNL1 preferentially bind to 3′ UTRs, indicating that this is a key function of both proteins in RNA processing. This suggests that the functional repertoire of MBNL1 should be expanded and that MBNL1, from being primarily regarded as regulator of alternative splicing, should also be considered as an important regulator of 3′ UTR-mediated processes, such as mRNA stability/degradation.

MBNL1 destabilize mRNAs. To analyze the function of CUGBP1/MBNL1 binding to 3′ UTRs, we made luciferase reporter constructs harboring CUGBP1/MBNL1-binding sites in the 3′ UTR. Since no CLIP tags were observed in the 3′ UTR of *Gapdh* (Supplementary Fig. S8), we made a *luciferase-Gapdh* 3′ UTR expression vector, and then inserted 12 repeats of GT and 7 repeats of CTG immediately after the stop codon of *luciferase* to introduce a CUGBP1-binding site (GU rich motif) and an MBNL1-binding site (YGCY motif), respectively (Fig. 4a). We also inserted 12 AC repeats as a control. Due to the high expression level of CUGBP1 in C2C12 cells we used HEK293 cells for transient transfection of these reporter constructs along with CUGBP1/MBNL1 expression vectors. For the constructs with *Gapdh* 3′ UTR alone or with AC repeats inserted, overexpression of CUGBP1 or MBNL1 had no effect on luciferase activity (Fig. 4b). For the GT repeat construct, overexpression of CUGBP1 decreased the luciferase activity, but MBNL1 had no effect. For the CTG repeat construct overexpression of MBNL1 dramatically decreased the luciferase activity, and also overexpression of CUGBP1 significantly reduced luciferase activity (Fig. 4b). In order to shed light on the mechanism underlying the observed decrease in luciferase activity we investigated the decay of *luciferase* mRNA. The SV40 promoter of the luciferase reporter constructs was replaced with a tet-repressible promoter, and HEK293 Tet-off cells were transiently transfected with these constructs. Doxycycline was added to the medium to stop transcription of the tet-responsive promoter, and the temporal profiles of *luciferase* and *GAPDH* mRNA levels were measured. Overexpression of MBNL1 together with the CTG repeat reporter construct resulted in highly increased decay of *luciferase* mRNA and CUGBP1 overexpression together with the GT repeat reporter construct also increased mRNA decay. Overexpression of either protein together with the *Gapdh* 3′ UTR control construct did not alter mRNA decay (Fig. 4c). These data demonstrate that binding of CUGBP1 and MBNL1 to the 3′ UTR promotes mRNA decay. To examine whether CUGBP1 and MBNL1 regulate decay of endogenous mRNAs, we next analyzed mRNA stability in actinomycin D treated C2C12 cells by expression arrays following siRNA knock down of CUGBP1 or MBNL1 (GEO accession number, GSE27583). To identify genes with reliable half-life estimates, we restricted our analysis to 195 transcripts using three conditions: (i) half-life between 2.5–5 hrs; (ii) correlation coefficient of fitting to an exponential decay greater than 0.9; and (iii) RMA-normalized signal values more than 100 at all time points. The median half-life of all the transcripts matching these criteria in the control is 3.56 hrs, whereas those from CUGBP1- and MBNL1-knocked down cells are significantly prolonged to 3.91 hrs and 3.73 hrs, respectively (Fig. 5a). We chose four additional representative mRNAs with a cluster of either CUGBP1- or MBNL1-tags in the 3′UTR, and confirmed by real time PCR that knockdown of either CUGBP1 or MBNL1 results in approximately two-fold increase in mRNA half-life of these target mRNAs (Fig. 5b). The half-lives of 100 out of 195 transcripts are prolonged both by knockdown of CUGBP1 and MBNL1, suggesting overlapping activity in the regulation of mRNA decay by CUGBP1 and MBNL1. We next analyzed the relationship between change in mRNA half-life and coverage of HITS-CLIP tags in the 3′ UTRs. We found that genes displaying prolongation of half-lives in response to CUGBP1 knockdown harbors more CUGBP1-tags in their 3′ UTRs, compared to those displaying shortening of half-lives (Fig. 5c). Similarly, genes that display prolongation of their half-lives in response to MBNL1 knockdown have more MBNL1-tags in their 3′ UTRs (Fig. 5c).

Gene Ontology analysis of CUGBP1/MBNL1-bound 3′ UTRs revealed that the terms 'cytoskeletal protein binding, 'transcription factor binding' and 'RNA binding' are significantly overrepresented for CUGBP1- and MBNL1-bound genes (Table 1).

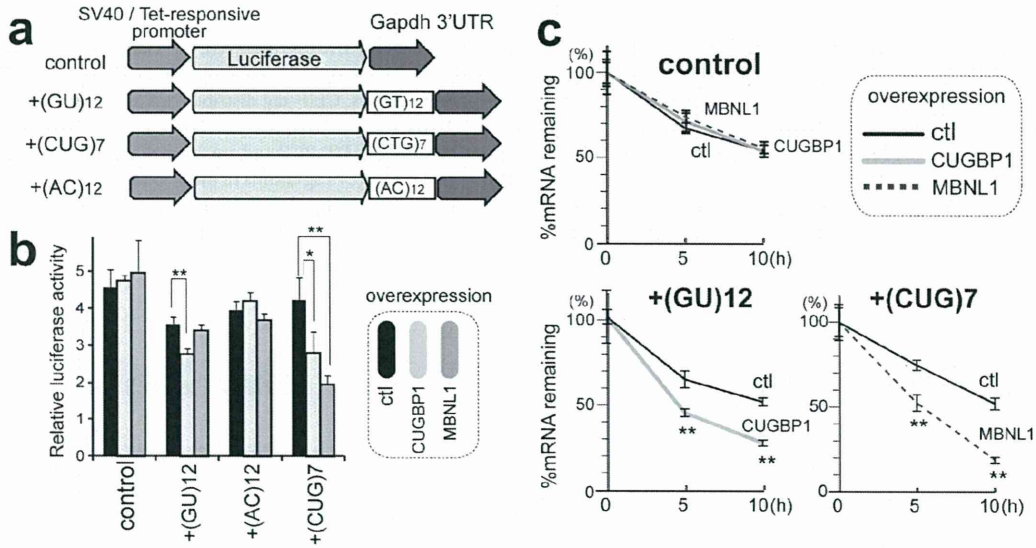

Figure 4 | Decay of *luciferase* mRNA by overexpression of CUGBP1/MBNL1. (a) Schemes of luciferase reporter plasmids harboring *Gapdh* 3′ UTR. Each construct was made carrying either SV40 or tet-responsive promoter. (b) Luciferase activity after overexpression of CUGBP1/MBNL1. HEK293 cells were transfected with the indicated SV40-driven luciferase reporter constructs. Luciferase activity is normalized for the transfection efficiency using co-transfection of pRL/SV40. (c) Decay of luciferase mRNA after overexpression of CUGBP1/MBNL1. HEK293 Tet-off cells were transfected with the indicated tet-responsive promoter-driven luciferase reporter constructs. Doxycycline was added to the medium to stop transcription at time 0. Temporal profiles of luciferase mRNA decay were quantified by real time RT-PCR and are normalized for *Gapdh* mRNA levels. All experiments were triplicated, and the mean and s.d. are indicated (* $p < 0.05$; ** $p < 0.01$).